Tectonic interactions during rift linkage: Insights from analog and numerical experiments

Timothy Chris Schmid[1], Sascha Brune[2,3], Anne Glerum[2], and Guido Schreurs[1]

[1]Institute of Geological Sciences, University of Bern

[2]Helmholtz Centre Potsdam – GFZ German Research Centre for Geosciences, Potsdam, Germany

[3]University of Potsdam, Potsdam-Golm, Germany

Corresponding author Timothy Schmid: timothy.schmid@geo.unibe.ch

Institute of Geological Sciences, University of Bern, Baltzerstrasse 1+3, CH-3012 Bern, Switzerland

Keywords: Numerical modelling, analog modelling, stress deflection, rift interaction, rift propagation

Abstract

Continental rifts evolve by linkage and interaction of adjacent individual segments. As rift segments propagate, they can cause notable re-orientation of the local stress field so that stress orientations deviate from the regional trend. In return, this stress re-orientation can feed back on progressive deformation and may ultimately deflect propagating rift segments in an unexpected way. Here, we employ numerical and analog experiments of continental rifting to investigate the interaction between stress re-orientation and segment linkage. Both model types employ crustal-scale two-layer setups where pre-existing linear heterogeneities are introduced by mechanical weak seeds. We test various seed configurations to investigate the effect of i) two competing rift segments that propagate unilaterally, ii) linkage of two opposingly propagating rift segments, and iii) the combination of these configurations on stress re-orientation and rift linkage. Both the analog and numerical models show counter-

intuitive rift deflection of two sub-parallel propagating rift segments competing for linkage with an opposingly propagating segment. The deflection pattern can be explained by means of stress analysis in numerical experiments where stress re-orientation occurs locally and propagates across the model domain as rift segments propagate. Major stress re-orientations may occur locally, which means that faults and rift segment trends do not necessarily align perpendicularly to far-field extension directions. Our results show that strain localization and stress re-orientation are closely linked, mutually influence each other and may be an important factor for rift deflection among competing rift segments as observed in nature.

1. Introduction

Continental rifting involves brittle faulting and the formation of subsiding rift basins. In places where individual rift segments are in proximity, they may interact and link when segments propagate and the rift system matures (Morley et al., 1990; Nelson et al., 1992; Rosendahl, 1987). The propagation and linkage of formerly isolated rift segments resembles the propagation and interaction of extension fractures on a micro-scale (e.g., Childs et al., 1995; Willemse, 1997; Willemse et al., 1996; Fig. 1a). Indeed, analytical solutions and models have been used to describe crack growth and to predict its direction (e.g., Macdonald and Fox, 1983; Mills, 1981). Such cracks occur in a variety of materials over a vast order of magnitude in length scale from micro-scale cracks in glass to km-scale ridge interaction structures in oceanic crust (Pollard and Aydin, 1984; Fig. 1a).

Propagation and interaction of individual rift segments occur in continental rift systems at various styles and scales (Fig. 1b) and have been intensively studied over the years. The East African Rift System (EARS) constitutes a narrow rift with an Eastern and Western branch that propagate southward and northward, respectively (EARS; e.g., Ebinger et al., 2000; Morley et al., 1990; Nelson et al., 1992; Bonini et al., 2005; Bosworth, 1985; Brune et al., 2017; Corti

et al., 2019; Glerum et al., 2020; Heilman et al., 2019; Koehn et al., 2008; Kolawole et al., 2018) comprising different sub-parallel deformed regions (inset Fig. 1c). On smaller scale, interaction of segmented grabens has been studied for example in in the Canyonlands National Park, Utah, a part of the Basin and Range wide rift (Allken et al., 2013; Trudgill, 2002; Schultz-Ela and Walsh, 2002), where various styles of graben interaction are attributed to the underlying strata (e.g., salt layer) or pre-existing weaknesses (Fig. 1d).
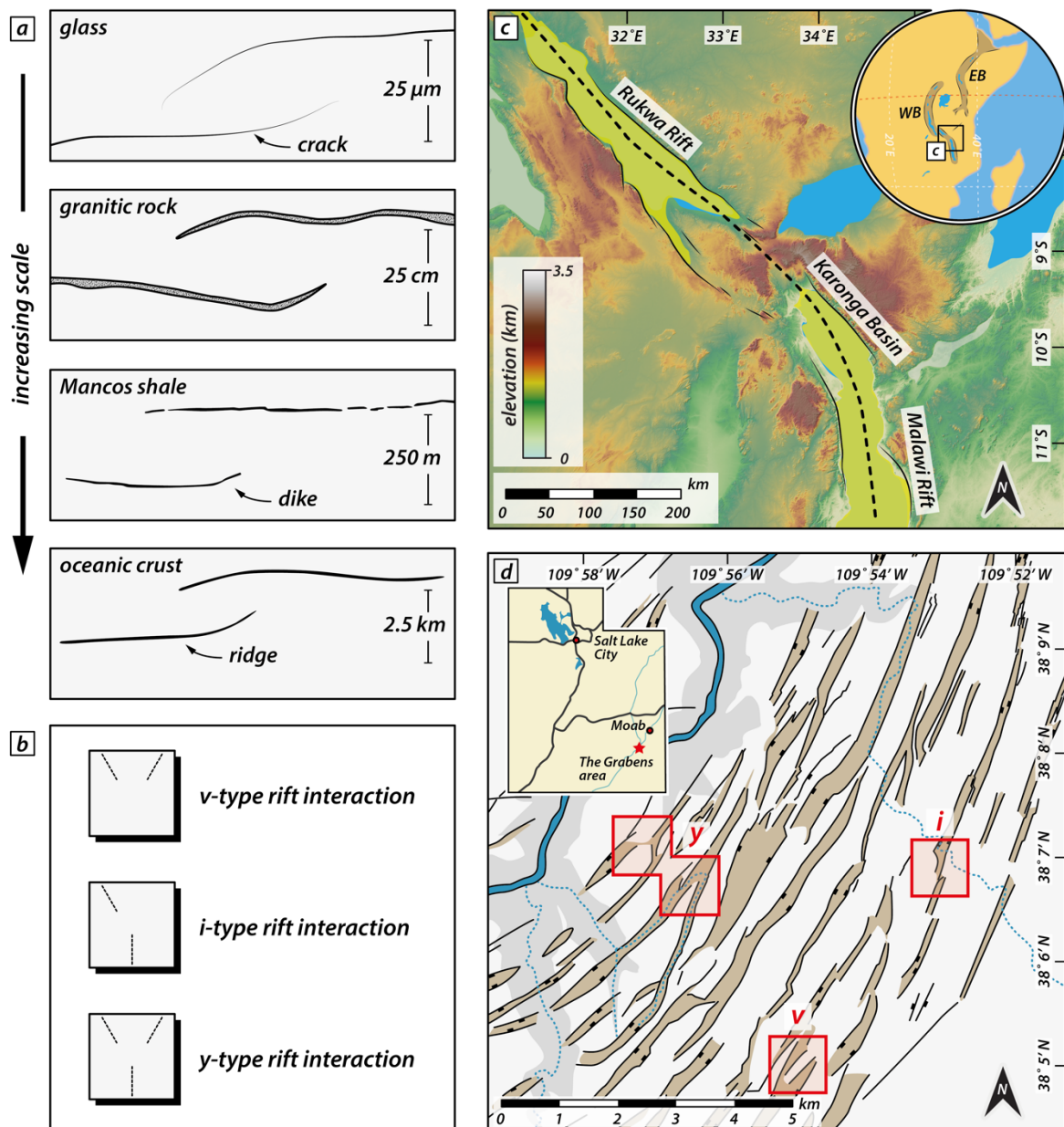
Figure 1: Similar linkage structures occurring at a vast range of spatial scales. a) Propagation and linkage of segments at different scale from micro cracks in glass to linkage of oceanic ridge segments. Redrawn after Pollard and Aydin, (1984). b) Rift-interaction types investigated in this study. c) Rukwa Rift and Malawi rift along the Western Branch of the East African Rift System (EARS; inset). The two basins link obliquely via the Karonga Basin and form an i-type interaction zone. Rift axis redrawn after Kolawole et al., (2021). WB: Western Branch; EB: Eastern Branch of the EARS. d) Rift-related linked graben structures in the Canyonlands National Park, USA. Red rectangles mark areas with distinct interaction geometries (v-, i-, and y-geometries; see b) and text for detail). Redrawn after Allken et al., (2013).

Structural inheritance is thought to control nucleation and strain distribution along newly formed normal faults as weak fabrics can precondition and weaken a heterogenous upper crust (e.g., Collanega et al., 2018; Heilman et al., 2019; Kolawole et al., 2018; Morley, 2010; Morley, 1999; Kolawole et al., 2021; Morley et al., 2004). Pre-existing weak fabrics may appear as large shear zones (Daly et al., 1989), suture zones along adjacent basement terranes (Corti, 2012; Corti et al., 2007) or upper crustal fabrics. Resulting rift structures may form as initially isolated segments that propagate along strike, interact and evolve into continuous zones of deformation with time as they link (Nelson et al., 1992). Rift segments link through previously un-rifted interaction zones resulting in a characteristic geometry that persists during later rift stages (Nelson et al., 1992).

Recent strain accommodation in the Rukwa-North Malawi segment of the western branch of the EARS (Fig. 1c) shows dominant dip-slip faulting parallel to the border faults (Kolawole et al., 2018; Morley, 2010) driven by the reactivation of pre-existing basement fabrics (Heilman et al., 2019). There, the concentration of seismicity in the SE and NW of the Rukwa and Northern Malawi Rift, respectively suggest subsequent propagation and linkage of the rift segments with a flip in the boundary fault polarity near the interaction zone (Heilman et al., 2019 and references therein).

90   Pre-existing structures as well as fault interaction across multiple scales disturb the regionally

91   inferred stress orientation (Morley, 2010; Oliva et al., 2022). In return, stress re-orientations

92   within and adjacent to rift segments influence the style of progressive deformation. Ultimately,

93   stress re-orientation may even favor pure dip-slip behavior even for extensional faults with an

94   oblique orientation to the regional extension (e.g., Morley, 2010; Corti et al., 2013; Morley,

95   2017; Philippon et al., 2015). This interplay between pre-existing structures and local re-

96   orientation of the regional stress field affects how propagating rift segments interact. Under

97   favorable conditions, it may even cause deflection of propagating rift segments (Nelson et al.,

98   1992).

99

100 Rift propagation and segment interaction has been investigated by analog modelling studies

101 that examined linkage of two segments across a transfer zone (e.g., Zwaan et al., 2016;

102 Zwaan and Schreurs, 2017; Corti, 2012; Acocella et al., 1999; Bellahsen and Daniel, 2005).

103 Bellahsen and Daniel (2005) studied the control of existing faults on new fault growth under

104 multiphase extension. They suggested that pre-existing faults may disturb the local stress field

105 and impede linkage of newly forming faults which also occurs in natural examples of

106 multiphase extension (Duffy et al., 2015). Such stress deflections have been reported and

107 studied in natural settings such as the North Malay Basin, Thailand, due to the vicinity of pre-

108 existing faults (Tingay et al., 2006; Tingay et al., 2010). While analog experiments are an

109 effective tool to simulate mechanical (brittle and ductile) deformation processes occurring in

110 continental rifts in 3D, accessing information about stresses is challenging. In contrast,

111 numerical modelling experiments provide direct access to element-wise stress tensors that

112 can be interpreted in terms of stress regimes and orientations under extension (Brune and

113 Autin, 2013; Duclaux et al., 2020). Despite the impact of stress distribution on faulting and

114 rift segment interaction, only recently numerical studies made use of it to gain further insights

115 into rift evolution and continental break-up (e.g., Glerum et al., 2020; Mondy et al., 2018).

116   However, these studies mostly focus on larger-scale deformation to evaluate stresses over the

117   entire time span of rifting up to continental break-up.

118

119   Here we use crustal-scale analog and numerical models to investigate rift propagation and

120   strain localization in early rifting stages when rift segments interact. Both types of models

121   document enigmatic rift segment deflection when two sub-parallel rift segments propagate

122   approximately in the same direction and compete for linkage with an opposingly propagating

123   segment. To understand the reason for rift segment deflection, we analyze the stress

124   distribution in early rifting stages and its interplay with strain localization that initiates above

125   pre-existing structures. Our experiments show that relatively simple rift segment interactions

126   can cause locally complex stress patterns that deviate from the regional stress field. Such

127   stress re-orientations occur in transient stages and can change over time and with progressive

128   deformation due to subsequent changes in material strengths.

129

2. Analog model

The presented analog modelling experiment shows unexpected features such as rift deflection. It motivates our numerical study, and we use the analog model as a reference for examining strain and stress distribution in numerical experiments.

2.1. Analog model setup

For the analog reference model, we use a simplified two-layer crustal scale setup with a brittle and a viscous material to simulate upper crustal brittle faulting and lower crustal viscous deformation, respectively. The base of the model consists of a set of alternating plexiglass and foam bars which are compressed prior to the model preparation by two mobile sidewalls (Fig. 2a). During the experiment the computer-controlled sidewalls extend and provide a symmetric extension gradient as the model base expands and the model vertically thins. For monitoring the surface deformation evolution, we use a stereoscopic camera setup to take top view photos and stereo image pairs every 60 s for quantitative deformation analysis by means of 3D stereo Digital Image Correlation (Adam et al., 2005). The model was scanned every 20 min in a medical XRCT scanner for gaining insights on internal model evolution.
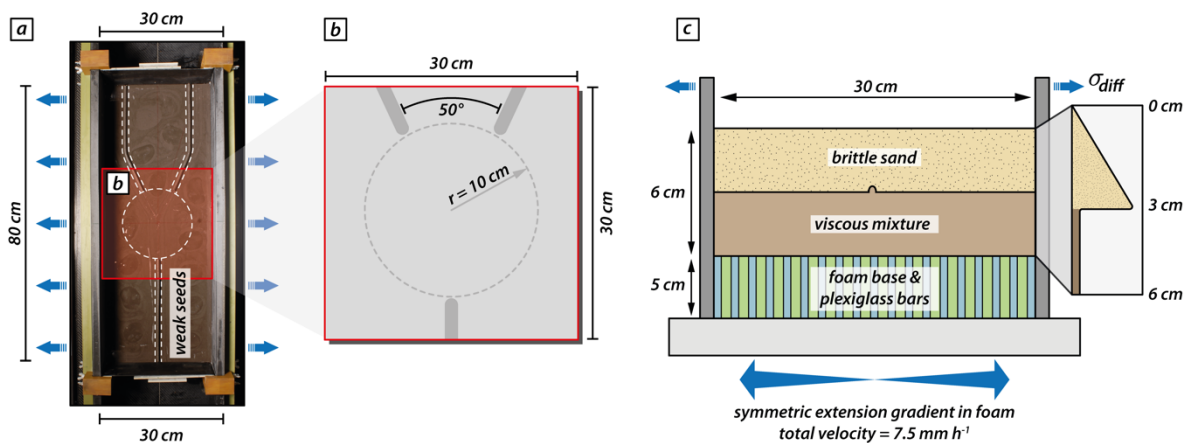
Figure 2: Analog modelling setup. a) Top view of the experimental apparatus with two mobile side walls that extend orthogonally. The entire model comprises an area of 80 x 30 cm and three viscous seeds are placed on top of the viscous layer before sieving in the brittle sand layer. The central model part where propagating rift segments interact contains no seeds.

156

2.2. Model geometry, rheological layering, and material properties

For simulating upper crustal deformation, we use dry quartz sand with a bulk density of 1560 kg m^{-3} and an internal friction coefficient of 0.72 (Schmid et al., 2020a). For the lower viscous model part, we use a quasi-Newtonian PDMS/corundum sand mixture (weight ratio 1:1) with bulk density of 1600 kg m^{-3} and a viscosity of $\sim 1 \times 10^5$ Pa s (Zwaan et al., 2018). Hence, the brittle-viscous setup has a density gradient that avoids density instabilities and spontaneous upwelling of the viscous layer. The model features viscous rods placed on top of the viscous model layer before sieving in the quartz sand (Fig. 2). These rods act as mechanically weak seeds and localize faulting in the upper brittle model domain. The used seed configuration includes three individual seed segments. The model includes a y-seed configuration with one seed segment perpendicular to the extension direction on one side (hereafter called frontal segment) whereas on the opposing side of the model center two obliquely placed seeds (hereafter called rear segments) form an intermediate angle of 50° (Fig. 2; see also Fig. 1b,d). The three seed segments hypothetically merge at the model center. However, we exclude weak seeds in an area with a radius r = 10 cm around the model center to allow free interaction of the propagating rift structures (Fig. 2b). The analog model comprises an initial area of 80 cm by 30 cm and has a total thickness of 6 cm (each layer 3 cm) which represents a 30 km thick continental crust. In accordance with the numerical setup, the effectively analyzed model area is restricted to 30 x 30 cm. The mobile sidewalls move with an extension velocity of 5 mm h^{-1} each (totaling in 10 mm h^{-1}), which results in a maximum extension of 40 mm at the final model stage after 4h.

178

2.3. Analog model results

In the analog model three different rift segments initiate above the weak seeds and propagate toward each other. Thereby, the two rear segments compete for linkage with the frontal segment. After 30 min (i.e., 5 mm extension; Fig. 3(i)), brittle deformation localizes along two rift boundary faults forming the frontal rift segment. Rifting in the rear segments localizes first along right-dipping rift boundary faults and after 60 min (i.e., 10 mm extension; Fig. 3(ii)) both rear segments develop a set of two conjugate rift boundary faults (Fig. 3a,b (ii)). Interestingly, instead of advancing straight forward, the fault tips deflect and propagate away from each other (Fig. 3b,d (ii)). This is partially due to the rift propagation over the area where no seeds are present where rifting perpendicular to the extension direction is favored. However, after 120 min (i.e., 20 mm extension; Fig. 3 (iii)) rift tips deflect and turn away from one another. Rift tips deflect from an initially oblique orientation and rotate into an inverted oblique direction (with respect to the extension direction). The frontal and the rear left rift segment propagate further and, as they approach one another, form an en-echelon basin that convergently overlaps with the frontal rift segment (Morley et al., 1990; Fig. 3b,d (iii)). After 180 min (i.e., 30 mm extension; Fig. 3(iv)), intra-rift faults develop in the frontal and left rear rift segments. Note that strain rate is successively localized in the two fully linked rift segments whereas the right rear segment experiences minor strain rate values (Fig. 3d (iv)). At the final model stage (i.e., after 240 min and 40 mm extension; Fig. 3 (v)), the right rear segment propagated minimally with a rift tip turned away from the linked segments (Fig. 3b,d (v)). The fully linked frontal and left rear segments continuously accommodated displacement resulting in deeper rift structures compared to the abandoned right rear segment (Fig. 3c,e (v)).
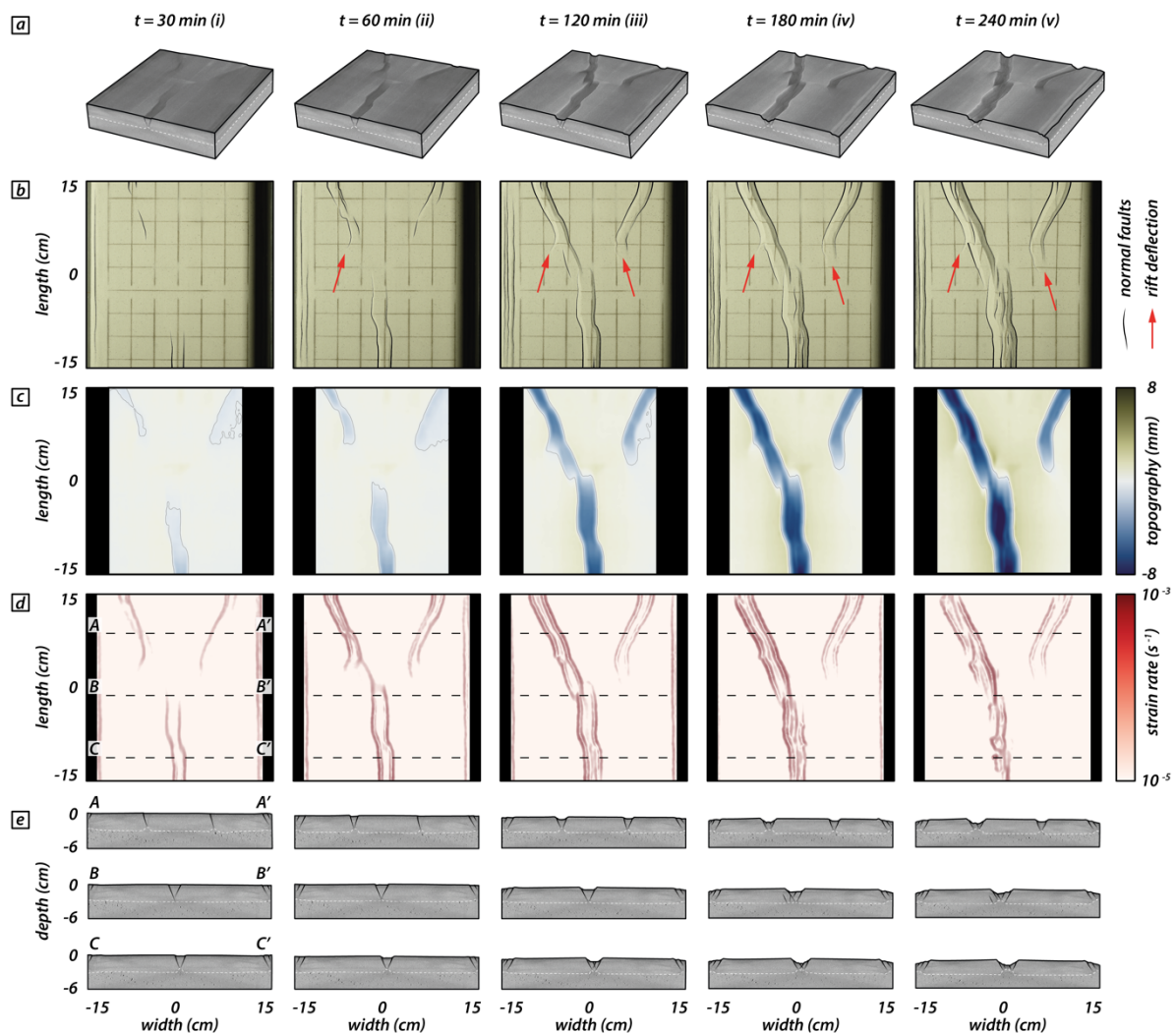
Figure 3: *Analog modelling results documenting deflection of the right rear segment and cessation of faulting activity. Distinct time steps (i.e., after 30 min and after every hour) show the model evolution. a) CT volumes of the investigated model domain at distinct time steps. White dashed lines indicate the brittle-viscous interface. b) Top views and line drawings indicating observable normal faults at the model surface. Red arrows indicate rift tips that deflect and turn away from one another. c) Topography from digital elevation models of the model surface. d) Strain rates obtained from 3D stereo DIC. Black dashed lines indicate positions of 3 transects through the CT volume. e) Rift transects A-A', B-B', and C-C'. White dashed lines indicate the brittle-viscous interface.*

3. Numerical modelling

We perform a series of numerical models to investigate rift linkage interaction and to analyze occurring surface stresses. Similar to the analog experiment, the numerical model consists of a two-layer crustal setup with laterally homogenous material layers where boundary-orthogonal extension with constant velocity is applied.

3.1. Numerical model setup

We use the open source, finite-element code ASPECT to solve the extended Boussinesq equations of momentum, mass, and energy in combination with advection equations for each compositional field (Gassmöller et al., 2018; Glerum et al., 2018; Heister et al., 2017; Kronbichler et al., 2012; Rose et al., 2017; Glerum et al., 2020). Since the numerical models are motivated by the analog model, the two setups are designed in a similar way. To this aim, we employ a numerical setup where the rheologies of upper and lower crust are brittle and ductile, respectively, and independent of temperature just like in the analog model. However, the numerical models operate on the true scales of the continental crust over tens of kilometers and millions of years, while the analog model is a scaled, cm-sized representation that evolves on hour-scale. Additionally, the numerical setup applies maximum extension velocities at the side walls and extension velocities at the base that linearly increase from the center towards the model boundaries. In contrast, maximum extension velocities at the side walls in the analog model are achieved via compression of a basal foam plexiglass setup (prior to the model run) that extends homogeneously during the model run.

The presented numerical experiments cover a rectangular cuboid domain of 150 km width and length in the horizontal x- and y-direction, respectively, and 30 km in depth along the vertical z-axis (Fig. 4a). The entire model domain is divided into 1.53 million hexahedral, second-order elements. For the upper 15 km of the model, we use a cell resolution of 750 m, with an additional refinement at the uppermost km which yields near-surface elements with a resolution of 375 m. The grid resolution for the lower 15 km of the model is 1500 m. At the left and right model sides, we apply a symmetrically distributed outflow velocity of $\frac{1}{2} V_x = 5$ mm yr^{-1}, resulting in a total extension velocity of 10 mm yr^{-1} (Fig. 4a,b). After a total model time of 4 My, the model has therefore experienced a total extension of 40 km. While V_x is prescribed at the left and right model sides, V_y and V_z are left free. We compensate material

243 loss through the side boundaries by compensational inflow at the model base and the

244 horizontal V_x component increases linearly from the model center towards the lateral model

245 boundaries (Fig. 4b). The front and back lateral boundaries allow for free slip and the top of

246 the model features a free surface boundary condition (Rose et al., 2017).

247

248 The model includes two rheological layers represented by compositional fields, namely a 15

249 km thick visco-plastic upper crust with a density of 2700 kg m^{-3} and a 15 km thick iso-viscous

250 lower crust with a density of 2900 kg m^{-3} and a constant viscosity of $1 \cdot 10^{20}$ Pa s. For the upper

251 crust, the viscous viscosity is fixed to $2 \cdot 10^{28}$ Pa s, such that plastic deformation is always

252 enabled. We introduce initial and dynamic mechanical weaknesses in the upper crust in two

253 ways. (i) Mechanically weak seeds: At distinct positions near the brittle-ductile interface, the

254 upper model layer is locally 10% thinned and the lower model layer elevates like the viscous

255 weak seeds in the analog model setup. These mechanical seeds weaken the upper crustal

256 strength and localize brittle faulting. Our experiments include three different seed

257 configurations: v, i, and y (Fig. 4c; see also Fig. 1b-d), where seeds within a central model

258 area (i.e., r = 100 km) are absent. For each configuration, the rear seeds form an intermediate

259 angle of 10°, 30°, or 50°. (ii) Friction softening: For each element, an initial plastic strain value

260 of 0 (resulting in strong material) to 0.1 (weaker) is randomly assigned and reduces the

261 maximum friction angle of 26.56° by a maximum of 10%. This reflects the structural

262 heterogeneity of natural settings and allows for more randomized strain patterns in the central

263 model domain where the mechanical seeds are absent. The initial plastic strain noise is

264 distributed over the entire model width with an amplitude following a Gaussian curve parallel

265 to the extension direction that is repeated along the model length (y-direction, Fig. 4d). During

266 continuous extension, the effective friction angle linearly reduces to 25% of the maximum

267 friction angle (i.e., to 6.64°) for plastic strain between 0 and 1 while it remains constant at

268 6.64° for plastic strains > 1 (Fig. 4e). This corresponds to a reduction of the effective friction

269   coefficient from 0.5 to 0.12. The cohesion of the upper crust remains constant at $5\cdot10^6$ Pa for

270   all conducted experiments.

271
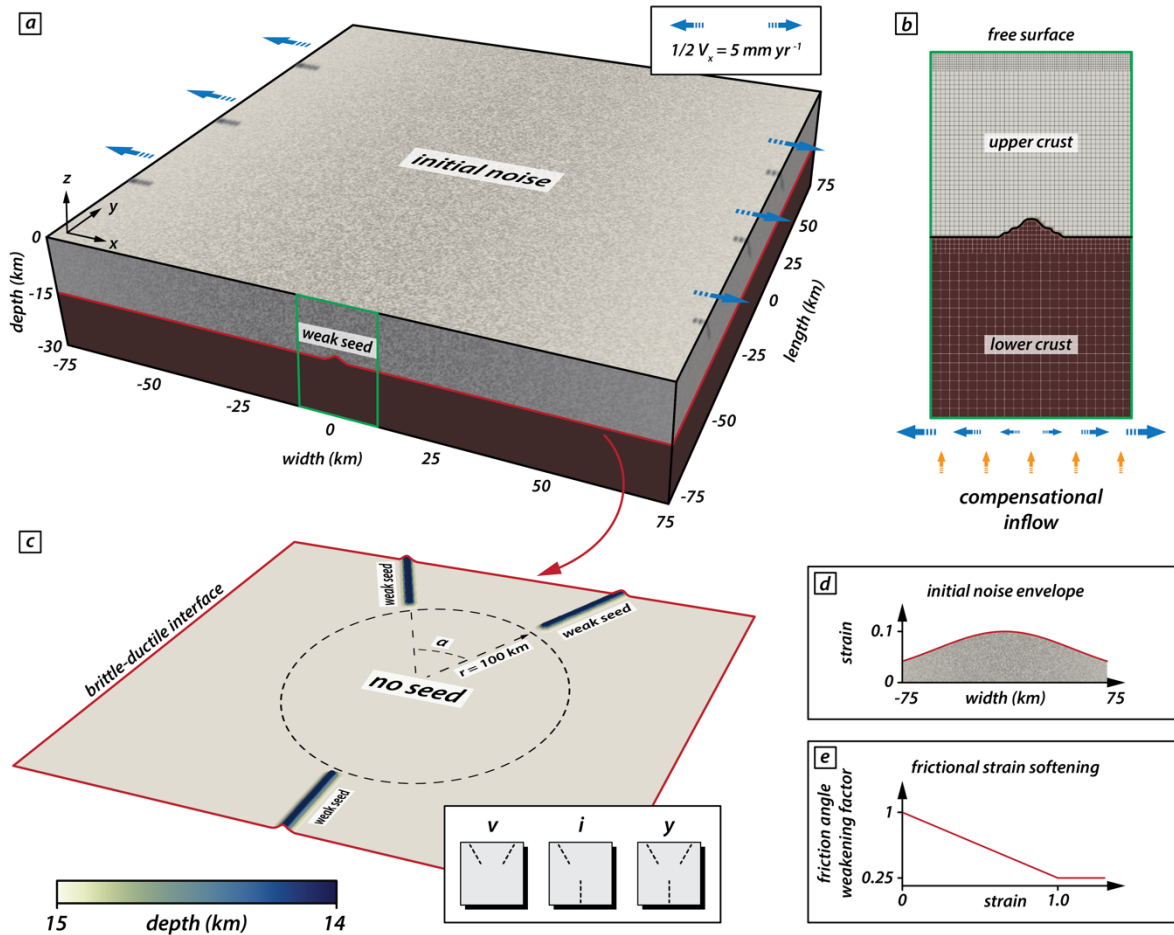
272
273
274   **Figure 4:** *Numerical model setup for iso-viscous models. a) The model domain comprises a volume of 150 x 150 x 30 km. Blue*
275   *arrows indicate the applied boundary-orthogonal extension. The green rectangle indicates the position of the zoom-in in b).*
276   *The red line indicates the initial depth of the brittle-ductile interface (as defined by the interface between the two rheological*
277   *layers) indicated in c). b) Initial conditions and mesh refinement (arrows not to scale). c) Position and configuration of the*
278   *mechanical weak seeds at the brittle-ductile interface. The setup comprises an area with radius r = 100 km where no weak*
279   *seeds are present. Three different seed configurations refer to y-, i-, and v-models (see text for details). d) Initial amplitude of*
280   *strain along the x-axis. The Gaussian distribution is constant along the y-axis; also see grey shade in a). Note that while the*
281   *strain amplitude follows a Gaussian distribution, the location of the initial strain is random. e) Linear weakening with strain*
282   *applied to the friction angle.*

283

3.2. Model limitations

Just like the analog model (Sec. 2), our crustal scale two-layer numerical setup does not comprise a lithospheric mantle layer and no asthenosphere. Further, the iso-viscous setup does not account for a temperature-dependent viscosity. However, we focus on an early rifting phase where the influence of the deforming mantle lithosphere can be neglected. The crustal-scale setup strongly limits the computational effort for calculating deformation in 3D (Allken et al., 2011, 2012; Katzman et al., 1995; Zwaan et al., 2016) and hence, our simplifications allow for a higher model resolution; a necessity to depict early stages of rifting and the coalescence of brittle deformation. Several alternative model runs have been performed including a temperature- and pressure-dependent viscosity. Those tests reproduced first-order features (i.e., strain rates, rift geometry and stress distribution) of the presented models in this study, which further justified the choice of a simplified iso-viscous setup. Note that we apply frictional softening as a function of strain within each cell. For simplicity, we do not include normalization accounting for cell size (Lavier et al., 2000) nor viscoplastic regularization techniques (Duretz et al., 2019; Jacquey and Cacace, 2020). Moreover, our model does not include the influence of melting or magma intrusions nor sedimentation and erosion.

3.3. Post-processing

Numerical models pose the advantage that they grant direct access to stress tensors of each individual cell. We exploit this opportunity by investigating surface stresses to deduct the stress regime and the effect of different seed configurations on stress distribution. ASPECT provides post processors that calculate the magnitude and orientation of the maximum horizontal stresses and the Regime Stress Ratio (RSR) (Glerum et al., 2020). This stress regime characterization is calculated according to the scheme of the World Stress Map (Zoback, 1992). The RSR value maps possible stress regimes to an interval between 0 and 3.

310 For isotropic and homogenous materials, the standard rules of Andersonian faulting are

311 applied (Anderson, 1905). For RSR values < 1, faulting occurs in an extensional stress regime

312 whereas for RSR values > 2 compressive stress regimes generate thrust faults. Strike-slip

313 faults occur for values $1 \geq RSR \leq 2$. We extract data of maximum horizontal compressive

314 stress together with the stress regime and investigate them in areas where the strain rate

315 exceeds a threshold of 10^{-16} s^{-1} and deformation occurs. For visualization, surface stresses

316 from an originally unstructured grid are resampled on an equidistant grid.

317

318 **3.4.   General model evolution of the reference model**

319 In this section we describe the numerical modelling results focusing particularly on the general

320 evolution of our reference model with a y-seed configuration and an intermediate seed angle

321 of 50° (Figure 5). At the early stage (i.e., after 0.5 million years), three distinct rift segments

322 develop above the initial seed positions bounded by a pair of conjugate rift boundary faults

323 (Fig. 5a (i)). This early stage is characterized by a symmetric evolution of the two competing

324 rear segments, which results in a symmetric subsidence inside of the graben structures (Fig.

325 5b (i)). For each rift segment, faulting activity is localized along the rift boundary faults. In

326 the central model domain, however, strain rates depict a more distributed deformation pattern

327 with multiple minor faults (Fig. 5c (i)). Note that the two rear segments propagate and show

328 curved fault segments that initially deflect and turn away from each other resulting in rift

329 segments with a curved geometry expressed in the topography (Fig. 5b (i)), similar to the rift

330 evolution in the analog model. Once they overlap with the propagating frontal segment, faults

331 symmetrically curve inwards and towards the frontal segment. The change from localized

332 strain rates above the seeds to distributed strain rate patterns in the central model domain is

333 best seen in transects (Fig. 5d (i)).

334

335   After the first million years, deformation has prominently localized along the left of the two

336   rear segments and along the frontal segment (Fig. 5a,c, (ii)). While deformation in the frontal

337   segment is localized along the rift boundary faults, inward migration occurred in the left rear

338   segment with developing intra-rift faults and only the left-dipping rift boundary fault active.

339   Similarly, the right rear segment shows faulting along the right-dipping rift boundary fault but

340   activity along intra-rift faults is lacking. In the central model domain, formerly distributed

341   deformation localized between the frontal and left rear rift segment (Fig. 5d (ii)). While strain

342   rates indicate a shift from a symmetric to an asymmetric deformation phase, topography is

343   still symmetric which implies that the shift is imminent and has not affected the topography

344   after the first million years (Fig. 5b (ii)).

345

346   After two million years, deformation is entirely localized along the frontal and left rear

347   segment. Only the right-dipping rift boundary fault of the frontal segment is active and inward

348   migration led to a set of pervasive intra-rift faults (Fig. 5a,c (iii)). The left rear segment depicts

349   a similar deformation pattern as in the previous step, but strain mainly accumulates along the

350   left-dipping rift boundary fault causing an asymmetric graben geometry (Fig. 5d (iii)). Note

351   that, after two million years, fault activity along the right rear segment completely ceased with

352   no further strain accumulation visible (Fig. 5a,c,d (iii)). The topography reflects this completed

353   switch from a symmetric to an asymmetric deformation stage with enhanced subsidence along

354   the frontal and left rear segments and their linkage throughout the central model domain (Fig.

355   5b (iii)).

356

357   With ongoing extension, deformation subsequently localizes along the axial rift zone that links

358   the frontal and left rear segments (Fig. 5a,c,d (iv,v)) and faulting activity along rift boundary

359   faults ceases. The linked structure reaches maximum depth inside of the rift after three million

360   years. After four million years, however, the basin experiences minor uplift due to increase

361   upward motion of the underlying viscous material (Fig. 5d (iv,v)). Note that the basin depth

362   of the right rear rift segment remains stable after two million years and does not experience

363   further subsidence nor uplift.

364

365
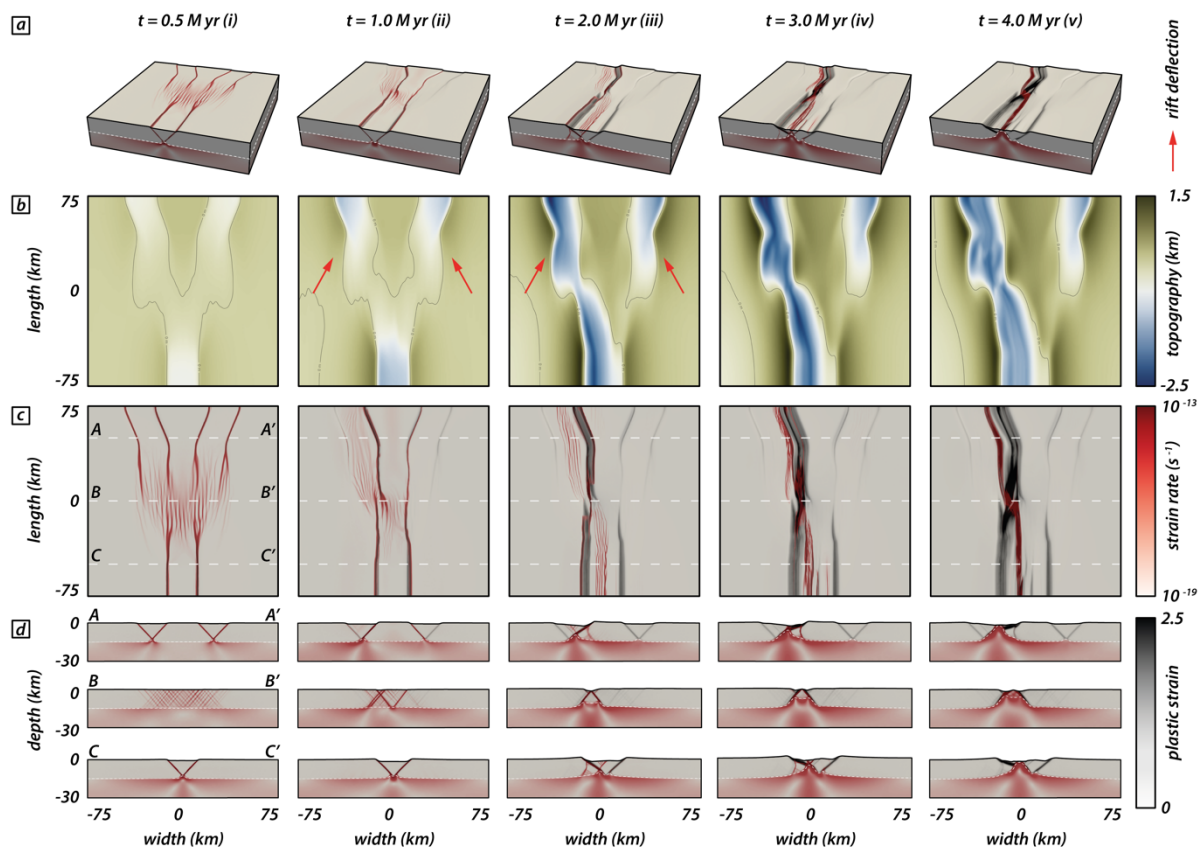
366
367   *Figure 5: Modelling results of the reference model documenting cessation of fault activity along the right rear segment while*

368   *the left rear and frontal segments link. Distinct time steps show the model evolution. a) Model box showing logarithmic strain*

369   *rates (red) and plastic strain (black) in the brittle and viscous model domain. White dashed lines indicate the brittle-viscous*

370   *interface. b) Top views showing the model topography. Red arrows indicate rift tips that deflect and turn away from one*

371   *another. Black lines refer to the zero-elevation height. c) Top views of the model showing strain rates (red) and corresponding*

372   *plastic strain (black) at distinct model run times. White dashed lines correspond to the three rift transects A-A', B-B', and C-C'*

373   *in subfigure d). d) Rift-axis perpendicular transects A-A', B-B', and C-C' parallel to the extension direction.*

374

3.5.   Early localization patterns for v-, i-, and y-seeds

376   To investigate the influence of different seed configurations, we compare v- (Fig. 6a-c), i-

377   (Fig. 6d-f), and y-seed (Fig. 6g-i) configurations for different intermediate angles (i.e., 10°,

378   30°, and 50°) at an early stage after 0.5 million years. y- and i-seed configurations provide a

379 setup where rift structures opposingly propagate towards the model center where rift linkage

380 eventually occurs. In contrast, rift structures in the v-seed configuration propagate

381 approximately in the same direction, which has a consequence on the overall strain rate

382 distribution.

383

384 The early stage in v-seed experiments (Fig. 6a-c) is characterized by a zone of localized and

385 distributed deformation in the rear and frontal part of the experiments, respectively. The

386 transition from localized to distributed deformation occurs where the two competing rift

387 segments deflect and rotate away from one another. Note that the fault deflection successively

388 decreases towards the left and right model sides, where faults strike perpendicular to the

389 extension direction. This is consistent with observations for experiments with a y-seed

390 configuration. However, there the two competing rear segments rotate back and eventually

391 bend towards the propagating frontal segment (Fig. 6g-i).

392

393 For experiment with a i-seed configuration (Fig. 6d-f) two opposingly propagating rift branches

394 form. Since the right rear segment is absent, both opposingly propagating rift segments link

395 in the model center where deformation is distributed onto intra-rift faults. The overall strain

396 rate field is localized, and no strain rate deflection occurs.

397

398 Models with a y-seed configuration (Fig. 6g-i) depict a strain rate pattern where deformation

399 is localized along rift boundary faults at the model margins where seeds are present and a

400 distributed en-echelon strain rate pattern in the model center. Note that for the model with

401 an intermediate angle of 10° the two competing rear segments are close enough resulting in

402 a zone where strain is localized along only one rift boundary fault per rift segment (i.e.,

403 outward-dipping faults with respect to the model box) that overlap and form a central graben

404 with minor intra-rift faults. For larger intermediate angles, two individual rift segments

405 (bounded by two rift boundary faults) form that propagate towards the model center. While

406 the strain rate pattern due to the competing rear segments is identical for experiments with

407 a y- and v-seed configuration, the additional frontal segment in experiments with a y-seed

408 configuration causes localization of strain rates in a single rift branch bounded by two rift

409 boundary faults. This contrasts with the v-seed configuration where strain rates in the frontal

410 model domain occur distributed over the entire model domain (Fig. 6a-c).

411

412
413
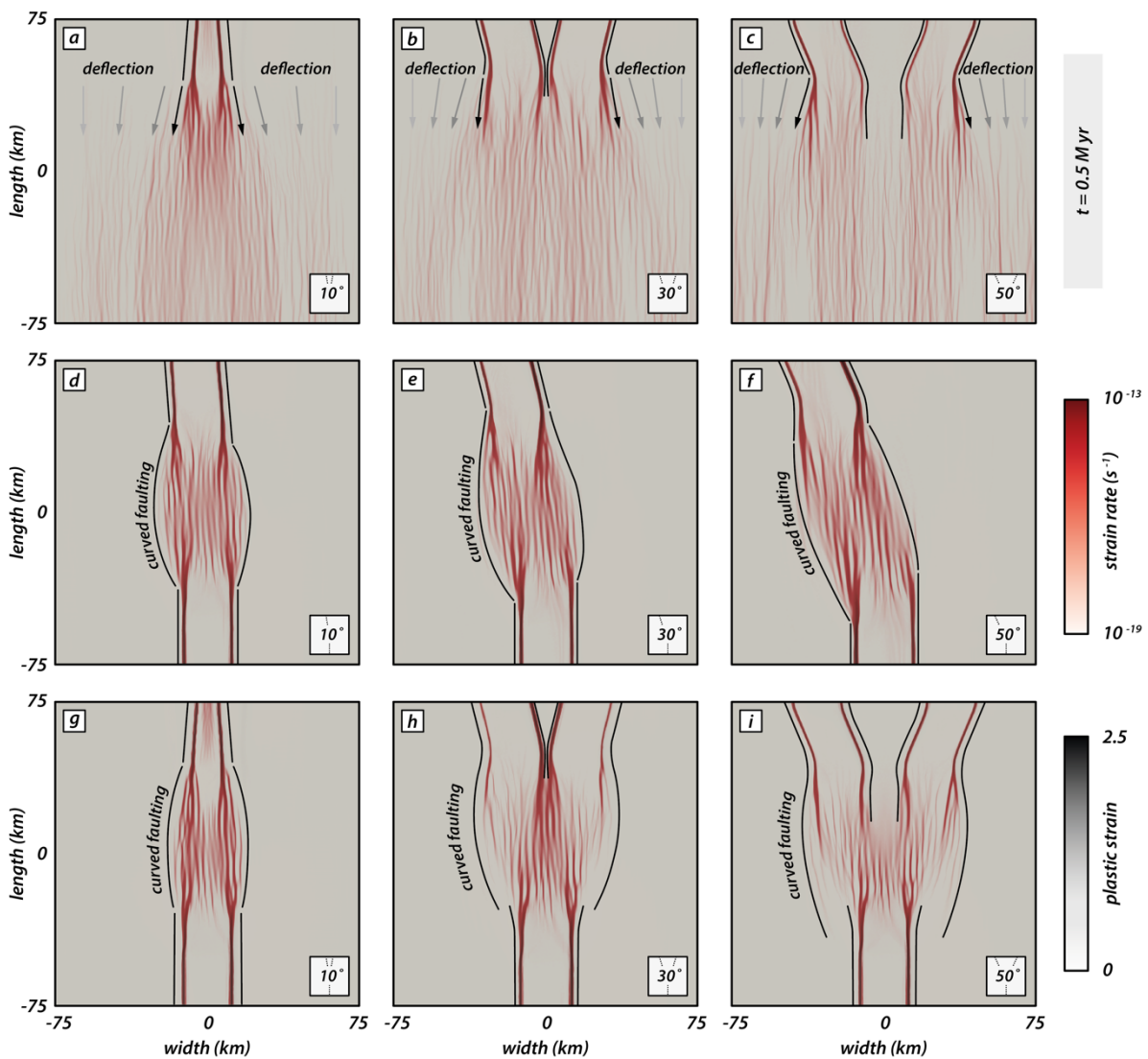
Figure 6: Types of rift segment linkages depending on the seed configuration at an early phase after 0.5 million years. Model

top views show strain rates (logarithmic) and plastic strain in red and black colors, respectively. a-c) v-seed configuration for

intermediate angles of 10°, 30°, and 50°. d-f) i-seed configuration for intermediate angles of 10°, 30°, and 50°. g-i) y-seed

configuration for intermediate angles of 10°, 30°, and 50° (reference model). Black lines confine deformed areas. For models

with a v-seed configuration (a-c), competing rift segments deflect away from each other resulting in a fan-shaped geometry. Note that fault strike successively re-orients into an orientation perpendicular to the extension direction towards the left and right model sides. Curved faulting occurs in models with an i- and y-seed configuration (d-j) where rift segments interact.

3.6. Final rift geometry and localization patterns for v-, i-, and y-seeds

The final model stage after four million years best illustrates differences in rift geometry between the models with different seed geometry and an intermediate angle (Fig. 7). Rift deflection is well visible in v-seed models (Fig. 7 a-c) and most prominent in experiments with a larger intermediate angle (Fig. 7b,c). Above the seeds, two short individual rift segments form bounded by a pair of conjugate rift boundary faults. However, as the rifts propagate towards the model center, strain is mainly accommodated along the boundary faults that dip towards the model center. Hence, the larger part of the model subsides uniformly and builds a broad rift zone confined by two large boundary faults. When the two rift segments propagate, they deflect and turn away from one another resulting in a gradually wider rift. For intermediate angles of 30° and 50°, both competing rift segments show active faulting along intra-rift faults in the rear model part, but a zone of continuous faulting activity has developed along the right side of the rift.

Models with an i-seed configuration show a continuous and straight rift geometry for all intermediate angles (fig. 7d-f). For an intermediate angle of 10°, the rift structure is nearly orthogonal with respect to the extension direction. Note that most plastic strain is accommodated along the left-dipping rift boundary fault (Fig. 7d). For larger intermediate angles, the rift subsequently experiences more segmentation with small left stepping segments towards the rear model part (Fig. 7e,f). Strain accommodation occurs mainly on the right-dipping rift boundary fault for the frontal model part and switches to the left-dipping boundary fault in the rear model part.
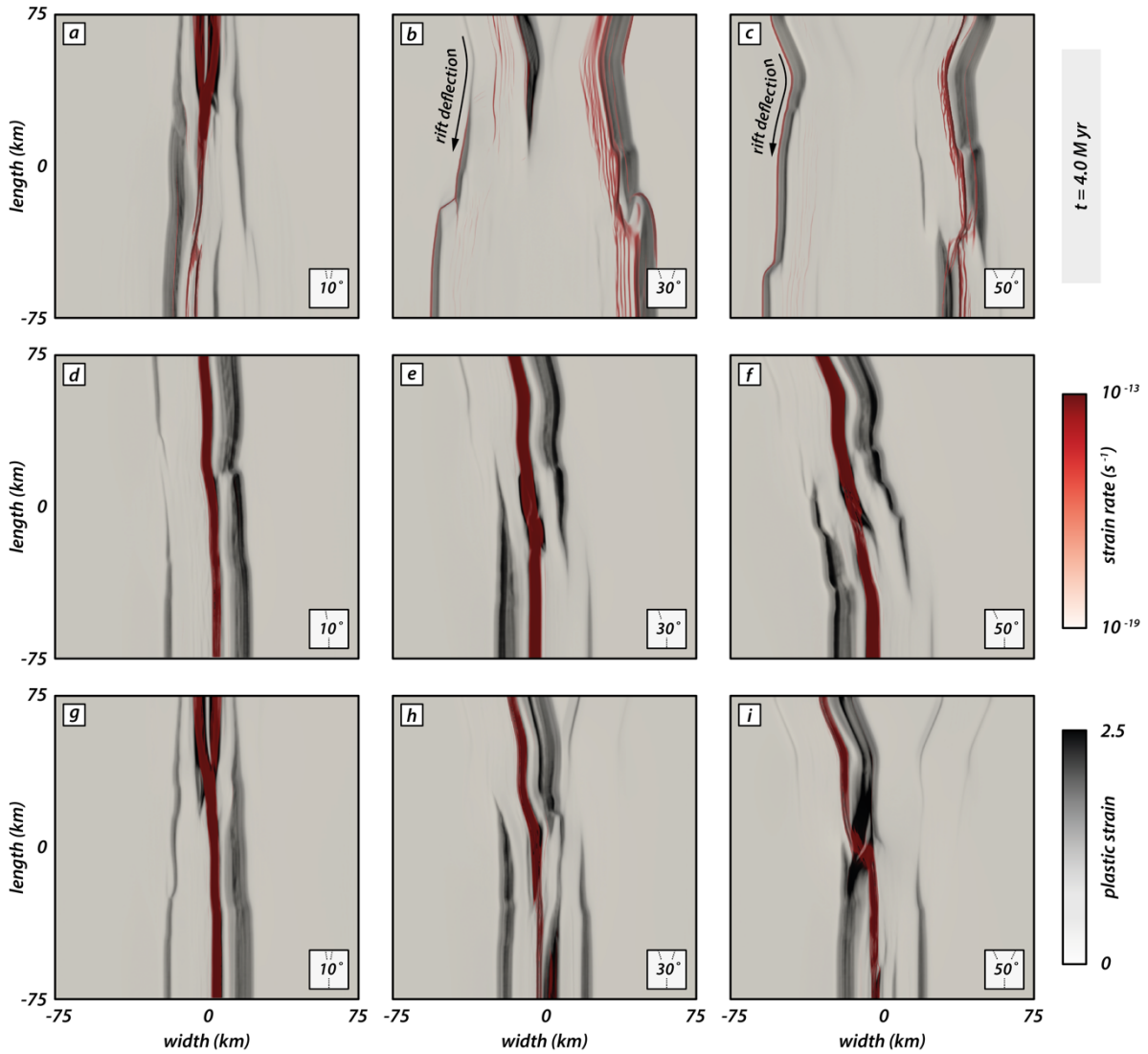
Figure 7: *Influence of seed configuration on the final rift geometry after 4 million years. Strain rates (logarithmic) and plastic strain are indicated by red and black colors, respectively. a-c) v-seed configuration for intermediate angles of 10°, 30°, and 50°. d-f) i-seed configuration for intermediate angles of 10°, 30°, and 50°. g-i) y-seed configuration for intermediate angles of 10°, 30°, and 50°(reference model).*

The most prominent difference occurs in models with a y-seed configuration and various intermediate angles. For an intermediate angle of 10°, the final rift geometry resembles that of a continuous straight rift segment (Fig. 7g). Both competing rear seeds are close enough such that they build one rift system rather than two distinct branches. For y-seed models with a larger intermediate angle (Fig. 7h,i), two individual rear rift segments form and compete for linkage with the frontal rift segment. Plastic strain well illustrates the asymmetric strain

457 accommodation focused along the left-dipping rift boundary fault of the left rear segment,

458 whereas the right rear segment only experienced minor strain accommodation (Fig. 7h,i). In

459 both cases, high strain rates are localized in the axial rift zone and witness activity along the

460 linked frontal and left rear segments.

461

462 Note that all experiments with an intermediate angle of 10° (Fig. 7a,d,g) form continuous

463 straight rift segments, regardless of the seed configuration. Additionally, the final rift geometry

464 for y- and v-seed configurations for an intermediate angle of 10° is similar with a gently wider

465 rift in the frontal model part (Fig. 7a,g). In contrast, for i-seed configurations the rift width is

466 similar along the entire length with a minor lateral offset (Fig. 7d). Strain rates are localized

467 in the axial rift zone throughout the entire model length forking into two close zones in the

468 rear end where the competing seeds are located.

469

470 **3.7. S_{Hmax} evolution with progressive deformation**

471 In this section we present the distribution and orientation of the maximal horizontal

472 compressive stress component S_{Hmax} with progressive rift evolution and segment linkage. We

473 focus on models with v-, i-, and y-seed configurations and an intermediate angle of 50° (Fig.

474 8; see also supplementary Figures S1-S3) distinguishing between model zones with pre-

475 existing structures (i.e., weak seeds) and a central zone where material strength is isotropic.

476

477 Our models depict two distinct phases within the first two million years: early strain

478 accommodation over a wider model domain followed by strain localization and linkage of

479 propagating rift segments (see also supplementary Figures S4-S6). Consequently, we focus

480 on S_{Hmax} in the first two million years of deformation and its effect on rift propagation. Figure

481 8 shows the orientation of S_{Hmax} and the stress regime based on the common color scheme of

482 the World Stress Map (Heidbach et al., 2018). Note that S_{Hmax} orientation and the stress regime

483   alone do not suffice to discriminate between locations where stresses exceed crustal strength

484   and faulting occurs. Strain rate values provide further necessary information, and we use a

485   threshold of 10^{-16} s^{-1} that splits the model into locations of active deformation (i.e., $\geq 10^{-16}$ s^{-1}

486   ^{1}) and tectonically inactive domains (i.e., $<10^{-16}$ s^{-1}).

487
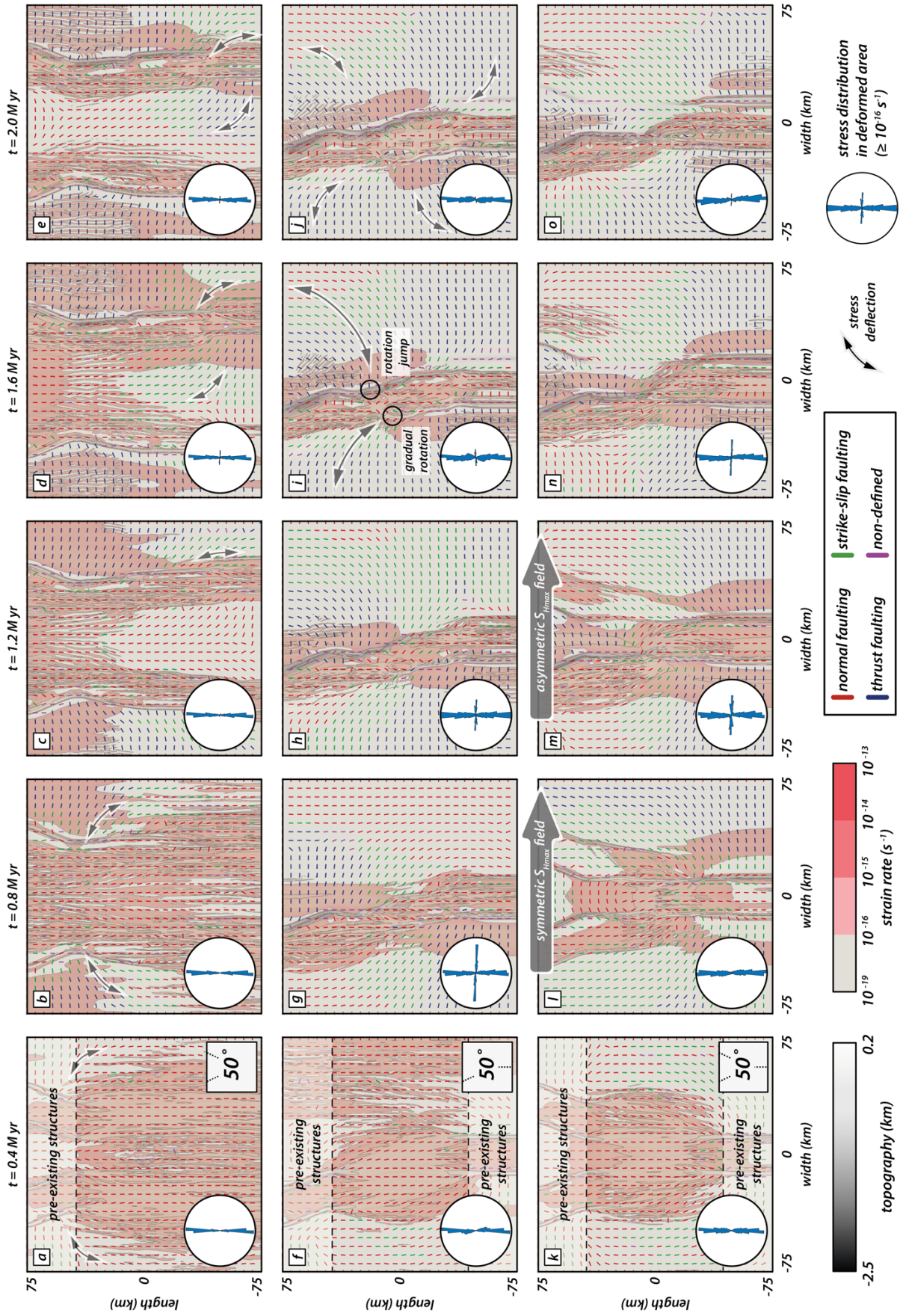
Figure 8: *Interplay of rift localization and surface stresses. Top views show the distribution of the maximum horizontal compressive stress component S_{Hmax} (not scaled to the magnitude) in models with an intermediate angle of 50° at early deformation stages (i.e., until 2 million years). a-e) v-seed configuration. f-j) i-seed configuration. k-o) y-seed configuration. Black colors refer to topographic elevation and red colors mark zones where strain rates exceed a threshold of 10^{-16} s^{-1}. Color coding for the stress regime marks normal, strike-slip, and thrust faulting in red, green, and blue, respectively, using the common color scheme of the World Stress Map (Heidbach et al., 2018). Elements where the stress regime is non-defined are marked purple. Black arrows highlight stress deflection of S_{max}. Rose diagrams show the distribution of S_{Hmax} orientation in zones where active faulting occurs (i.e., strain rate ≥ 10^{-16} s^{-1}). Large grey arrows for the y-seed configuration mark the change from a symmetric to an asymmetric S_{Hmax} distribution.*

3.7.1. Effect of S_{Hmax} re-orientation on rift propagation of competing rift segments (v-seed models)

Early stages in our numerical experiments are characterized by rift deflection and curved fault traces in the model center where rift segments interact (see Fig. 6). Hereafter we refer to that phenomenon as arcuate faulting. Arcuate faulting mainly occurs in experiments with larger intermediate angles (>10°) in early stages (Fig. 6), especially if two competing rift segments are present (v-, and y-seed configurations). Moreover, we have shown that deflection of propagating rifts occurs when deformation is symmetrically distributed along both competing rift branches. This is clearly visible for the v-seed configuration (Fig. 8a-e). Assuming orthogonal extension and isotropic material properties, S_{Hmax} is expected to align perpendicular to the extension direction producing pure dip-slip normal faults (Anderson, 1905). However, the model shows an immediate S_{Hmax} re-orientation at early deformation stages (i.e., after 0.4 million years; Fig. 8a) from a N-S to a E-W orientation in the vicinity of the underlying weak seeds such that dip slip faults are favored over oblique-slip faults with a strike-slip component. With progressive extension (Fig. 8b-e), S_{Hmax} re-orientations successively propagate into the isotropic zone without pre-existing structures, concomitant with the rift propagation. Consequently, the position of the front where stress rotation occurs propagates over time resulting in the deflection of the propagating rift arms away from each other.

519   There is a distinct difference between stress deflection along weak structures and E-W

520   deflections of S_{Hmax} in zones where strain rates are below the set threshold of 10^{-16} s^{-1}. The v-

521   seed configuration shows localized strain accumulation along one rift boundary fault per

522   segment (i.e., the outer one) resulting in a rift zone with a broad graben system that subsides

523   (Fig. 8e). S_{Hmax} re-orientation inside of the graben is in parts identical to the E-W orientation

524   of S_{Hmax} outside of the graben. While local S_{Hmax} rotations may be explained by small

525   differences in the maximum and intermediate principal stress components, such E-W stress

526   re-orientation in our model occurs systematically and suggest that this feature reflects the

527   influence of the strength anisotropy (Morley, 2010). The initial S_{Hmax} deflection near weak

528   structures locally favors dip-slip faulting but also has regional influence on the overall stress

529   regime.

530

531   **3.7.2. S_{Hmax} evolution in sub-parallel rift segments (i-seed models)**

532   During the early stage (i.e., after 0.4 million years, Fig. 8f), the distribution of S_{Hmax} resembles

533   the distribution from the v-seed configuration described in the previous section. Stress

534   deflection mainly occurs in zones where a weak fabric is present. S_{Hmax} values in the central

535   zone rotate by a small amount and reflect arcuate faulting (see Fig. 6). Since the two rift

536   segments propagate in opposing directions, linkage is efficient and localizes in a short time

537   (Fig. 8f-j). S_{Hmax} values deflect accordingly along propagating faults, which affects the entire

538   model domain. This deflection does not occur symmetrically on both sides of each rift segment.

539   Rather, it shows two distinct zones: 1) E-W orientations outside the rift deflect into a parallel

540   orientation near the rift boarder or 2) N-S orientations outside of the rift deflect into E-W

541   orientations near faults (Fig. 8j).

542

543   We find that S_{Hmax} orientations deflect gradually from E-W to N-S along abandoned rift

544   boundary faults where activity ceased (Fig. 8h-j; upper left and lower right model domain). In

545   contrast, S_{Hmax} re-orientations from N-S to nearly E-W towards active rift boundary faults are

546   followed by a rapid flip back to N-S along the faults (Fig. 8h-j; lower left and upper right model

547   domain). The two types of re-orientation seem to correspond with two types of deformed

548   zones. Where deformation is strongly localized along rift boundary faults, jumps in the S_{Hmax}

549   orientation occur. In contrast, zones where inward migration of fault activity activates intra-

550   rift faults, S_{Hmax} re-orientation occurs gradually.

551

552   ### 3.7.3. Rift arm competition and deflection (y-seed models)

553   A prominent feature in our models with two competing rift segments is the deflection of rift

554   branches and arcuate strain rate patterns (Fig. 8a-e) in the model with a v-seed configuration.

555   Moreover, the i-seed configuration demonstrates a gradual S_{Hmax} re-orientation over a broader

556   pre-weakened zone due to formerly active boundary faults. One could therefore expect that

557   both features should occur in the model with y-seed configuration (Fig. 8k-o).

558

559   Indeed, early stages (i.e., after 0.4 million years; Fig. 8k) are characterized by a symmetric

560   stress field with re-oriented S_{Hmax} values near the two rear rift segments. However, in contrast

561   to the v-seed configuration, S_{Hmax} re-orientation also occurs near the frontal pre-existing weak

562   fabric along developing rift boundary faults. In the isotropic zone, S_{Hmax} values dominantly

563   show a N-S direction. The general N-S orientation reflects the regional stress field due to an

564   E-W extension as predicted by Anderson (1905) in isotropic areas, into which rift segments

565   have yet to propagate. With ongoing extension, all three rift segments propagate into the

566   isotropic zone and cause a re-orientation of S_{Hmax} (Fig. 8l). Note that after 0.8 million years

567   the stress re-orientation occurs symmetrically. This contrasts with the i-seed configuration

568   where S_{Hmax} values deflect into either an E-W orientation along active rift boundary faults or

569   gradually turn into a fault parallel direction over a broader weakened zone (see subsection

570   3.7.2.). The early symmetric stress distribution in the y-seed configuration model is

571 unarguably due to the symmetric seed configuration (see also Fig. 8a-e). At this stage, dip-

572 slip faulting along the competing sub-parallel rift segments is favored over oblique slip faults

573 as in models with a v-seed configuration. It is only after 1.2 million years, when fault activity

574 along the right rear segment ceases that deformation localizes along the left rear and frontal

575 segments and linkage intensifies (Fig. 8m). Successively, localization and linkage occur

576 coevally with a switch from a symmetric to an asymmetric stress distribution and resembles

577 more the stress distribution in the i-seed configuration model (Fig. 8f-j). The model state after

578 1.2 million years (Fig. 8m) also marks the switch from a symmetric to an asymmetric stress

579 distribution that was formerly dominated by the competing rear rift segments with dip-slip

580 faulting favored along the two competing rift segments (see also v-seed configuration; Fig. 8

581 a-e). After 1.2 million years the system is dominated by the linkage of two obliquely oriented

582 segments (i.e., i-seed configuration). Note that after 1.2 million years dip-slip faulting mostly

583 occurs along the competing rift segment that links with the opposingly propagating segment

584 whereas dominantly oblique slip faults occur along the abandoned rift segment where activity

585 ceases.

586

587 The symmetry switch is also visible in rose diagrams of stress orientations within the active

588 faulting zone (i.e., strain rate $\geq 10^{-16}$ s^{-1}). A dominantly N-S oriented S_{Hmax} distribution changes

589 to a bimodal distribution with a second E-W orientation (Fig. 8l-n). Similarly, bimodal S_{Hmax}

590 distribution is also visible in the experiment with an i-seed configuration but occurs earlier.

591 Since the experiment with an i-seed configuration is never in the state of an early symmetric

592 stress distribution linkage is facilitated and occurs earlier (Fig.8g-i).

593

594 ## 4. Discussion

595 Despite the relatively simple setup of our experiments, the interaction of individual weak seeds

596 generates a complex evolution of linkage patterns. In the following we discuss the effect of

597   pre-existing structures on S_{Hmax} re-orientations and how, in return, stress re-orientation

598   influences rift propagation and rift segment linkage.

599

4.1.   Effect of pre-existing structures on rift segment propagation,

interaction, and S_{Hmax}

602   Previous modelling studies demonstrated that pre-existing weaknesses may cause local re-

603   orientations of S_{Hmax} resulting in extensional faults with an oblique orientation to the regional

604   extension direction which exhibit pure dip-slip behavior (e.g., Morley, 2010; Corti et al., 2013;

605   Morley, 2017; Philippon et al., 2015). This contrasts the expected (assuming Andersonian

606   faulting theory) occurrence of faults with an oblique slip component above pre-existing

607   structures that are obliquely oriented with respect to the extension direction (Tron and Brun,

608   1991; Withjack and Jamison, 1986). Our S_{Hmax} analysis documents two types of stress re-

609   orientation, either gradually or by a jump along faults (Fig. 8i). A potential explanation for the

610   two types of stress deflection is that cessation of boundary fault activity (and subsequent

611   faulting activity along intra-rift faults) creates a broad zone of reduced crustal strength. Hence,

612   S_{Hmax} orientations successively re-orient along those formerly active faults and eventually

613   rotate into a N-S orientation along active intra-rift faults. In contrast, where faulting activity

614   is strongly localized along rift boundary faults, re-orientation occurs rapidly by a jump from E-

615   W to a N-S orientation. This suggests that formerly active faults act as a wider zone of pre-

616   weakened material, where stresses deflect sequentially rather than with a rapid jump. Similar

617   observations have been made in previous studies of numerical models (Gudmundsson et al.,

618   2010; Kattenhorn et al., 2000). These experiments suggest that earlier fractures lead to

619   subzones (within a broader damage zone), where stresses subsequently rotate away from the

620   regional stress field. Although our analog and numerical models do not feature elastic

621   deformation, they indicate that stress deflection is an ongoing process, even after elastic

622   material failure. Such a stress deflection further implies that stress orientations in rocks with

623   pre-existing weaknesses can substantially deviate from predicted orientations in isotropic

624   media (Anderson, 1905).

625

626   It has been proposed that early faulting and propagation in the Rukwa and North Malawi Rifts

627   (Fig. 1c) were guided by pre-existing basement fabrics (Heilman et al., 2019). This region is

628   further shaped by a flip in the boundary fault polarity in the present-day geometry within the

629   interaction zone between Rukwa Rift and North Malawi Rift (Bosworth, 1985). Our i-seed

630   models show identical geometries for increasing intermediate angles (Figs. 7h,i and S5), where

631   plastic strain near pre-existing structures is mostly accommodated along prominent rift

632   boundary faults that flip fault polarity from the frontal to the rear rift segment. This flip in

633   fault polarity occurs prominently in models with an intermediate angle $\geq 10°$. We speculate

634   that the increasing obliquity of the southward propagating rift segment favors asymmetric

635   graben evolution with one dominant boundary fault accommodating a larger amount of strain.

636   In contrast to small intermediate angles (i.e., $10°$), seed configurations with a higher obliquity

637   provoke local rotation of S_{Hmax} within the interaction zone into a strike-slip regime near the

638   subordinate boundary fault (Fig. S5). Hence, strain accommodation along incipient faults

639   within the dip-slip regime is favored. This facilitates propagation along those dominant rift

640   boundary faults and eventually defines the final rift geometry.

641

642   Kolawole et al. (2018) further propose two different types of strain accommodation at early

643   rift phases. Prominent strain accommodation localized onto a discrete and narrow zone along

644   large rift boundary faults (Style-1; sensu Kolawole et al., 2018) and faulting distributed over

645   a broader zone, where fault clusters may reflect pre-conditioning of the material (Style-2;

646   sensu Kolawole et al., 2018). With this perspective, jumps and gradual rotation of S_{Hmax}

647   orientations are comparable to Style-1 and Style-2 strain localization, respectively, as

648   proposed by Kolawole et al. (2018). Hence, the type of weakness (narrow discrete zone or

649 distributed cluster zone) should also be reflected by the stress re-orientation distribution

650 (Morley, 2010).

651

4.2. Local S_{Hmax} re-orientation and its influence on rift segment interaction

653 **and rift deflection**

654 A particular observation in our experiments with a v-, and y-seed configuration is that two

655 sub-parallel rift segments, which propagate approximately in the same direction deflect away

656 from each other at early stages. This is somewhat surprising as one would expect the two rift

657 segments to cut towards each other by minimizing fault length. The occurrence of rift

658 deflection in both analog and numerical experiments validates that the results are robust and

659 require discussing the role of S_{Hmax} re-orientation and how it influences rift segment

660 interaction.

661

662 We speculate that, while both rear rift segments in our y-seed models equivalently

663 accommodate strain in the early stages (i.e., when the overall stress distribution is symmetric;

664 Fig. 8), S_{Hmax} orientations are dominated by the influence of the two competing rear rift

665 segments that accommodate strain in equal parts. It is only after fault activity along one rear

666 segment ceases that deformation localizes along the active rear and frontal segments and

667 linkage intensifies. Strain localization and linkage occur coevally with a switch from a

668 symmetric to an asymmetric stress distribution resembling the stress distributions in v-, and

669 i-seed configuration models, respectively. The switch from a symmetric to an asymmetric

670 stress distribution in y-seed models also marks the switch from a system that was formerly

671 dominated by the competing rear rift segments (i.e., v-seed configuration) to a system that

672 is dominated by the linkage of two obliquely oriented segments (i.e., i-seed configuration).

673

674   In models with a v-seed configuration, however, the symmetric phase prevails and causes

675   coeval S_{Hmax} re-orientations and rift deflection that cause divergence of the two propagating

676   rift segments. A similar process of extensional segment interaction via stress rotation is known

677   from mid-ocean ridge settings: Pollard and Aydin (1984) argue that paths of two opposingly

678   propagating oceanic ridges weakly diverge due to shear stresses that divert propagating ridges

679   as they approach each other. Once the two ridges overlap, the stress field changes causing

680   convergence and intersection. Similarly, Nelson et al. (1992) describe interference of

681   compressional zones of propagating cracks diverting their tips before they overlap and turn

682   back toward another. In this respect, our models with a v-seed configuration suggest that

683   stresses also cause divergence of two rift segments that propagate approximately in the same

684   direction. However, overlap never occurs (as they propagate approximately in the same

685   direction) and hence, the two segments remain in a stress field that further diverts their paths.

686

687   Only in models with a y-seed configuration, compressional zones and rift deflection can be

688   overcome once the opposingly propagating rift segment links with one of the competing rift

689   segments. Linkage occurs after about the first million years, concurrently with rift deflection

690   and abandonment of the right rear segment (Figs. 9a and S6). Moreover, remaining activity

691   in the right rear segment depicts low strain rates along numerous arcuate intra-rift faults (Figs.

692   9b and S6). This suggests that linkage and rift abandonment are closely coupled and faulting

693   along the linked segments intensifies when the activity along the remaining rift segment

694   ceases. In addition, the left rear segment displays a rather asymmetric half graben geometry

695   (Figs. 5c,d, 7i and S4) with one prominent rift boundary fault accommodating a larger part of

696   plastic strain similar to our models with a i-seed configuration (see also Figs. 7e,f and S5).

697   Dominant strain accommodation occurs along the west-dipping rift boundary fault of the left

698   rear segment coinciding with jumps in the S_{Hmax} orientation (Fig. 8m-o). Our modelling results

699   show that stress deflection along rift segment tips is a mechanical consequence of the

700   interaction between weak zones and far-field stresses offering a potential explanation for

701   naturally occurring rift deflection. However, we must emphasize that complexities in natural

702   rift settings pose additional difficulties that require further investigations of stress orientations.

703

704   An example of rift deflection in nature has been described in the Main Ethiopian Rift.

705   Geophysical and geologic studies evidence that pre-existing structures controlled the

706   approximately 11 Ma southward propagation of the Northern Main Ethiopian Rift and its

707   contemporaneous westward deflection along the Yerer-Tullu Wellel Volcanotectonic

708   Lineament (YTVL; Abebe et al., 1998; Keranen and Klemperer, 2008; Muhabaw et al., 2022).

709   Only after the rotation of the principal stress direction at about 5-6 Ma (Bonini et al., 2005),

710   extension along the YTVL ceased and deformation localization along the Central Main

711   Ethiopian Rift became more favorable. Our models document similar rift deflections and

712   moreover indicate that, even in the absence of changing plate motions, rift segments deflect,

713   and may cease while competing rift segments prevail and strain further localizes.

714

715   For the Canyonlands National Park, it has been proposed that it is mainly the lateral offset

716   between pre-existing structures that explains the diversity of structures (Allken et al., 2013;

717   Fig. 1d). With larger offsets, interaction between adjacent rift segments is limited and

718   competing grabens persist and endure ongoing propagation coevally. We find that stresses,

719   in combination with the geometry of pre-existing structures, play an important role and that

720   they have a mutual effect on one another. Hence, stress distribution must be considered as

721   an important factor especially in early rifting stages when segments link and predetermine

722   strain localization during subsequent progressive rifting.

723
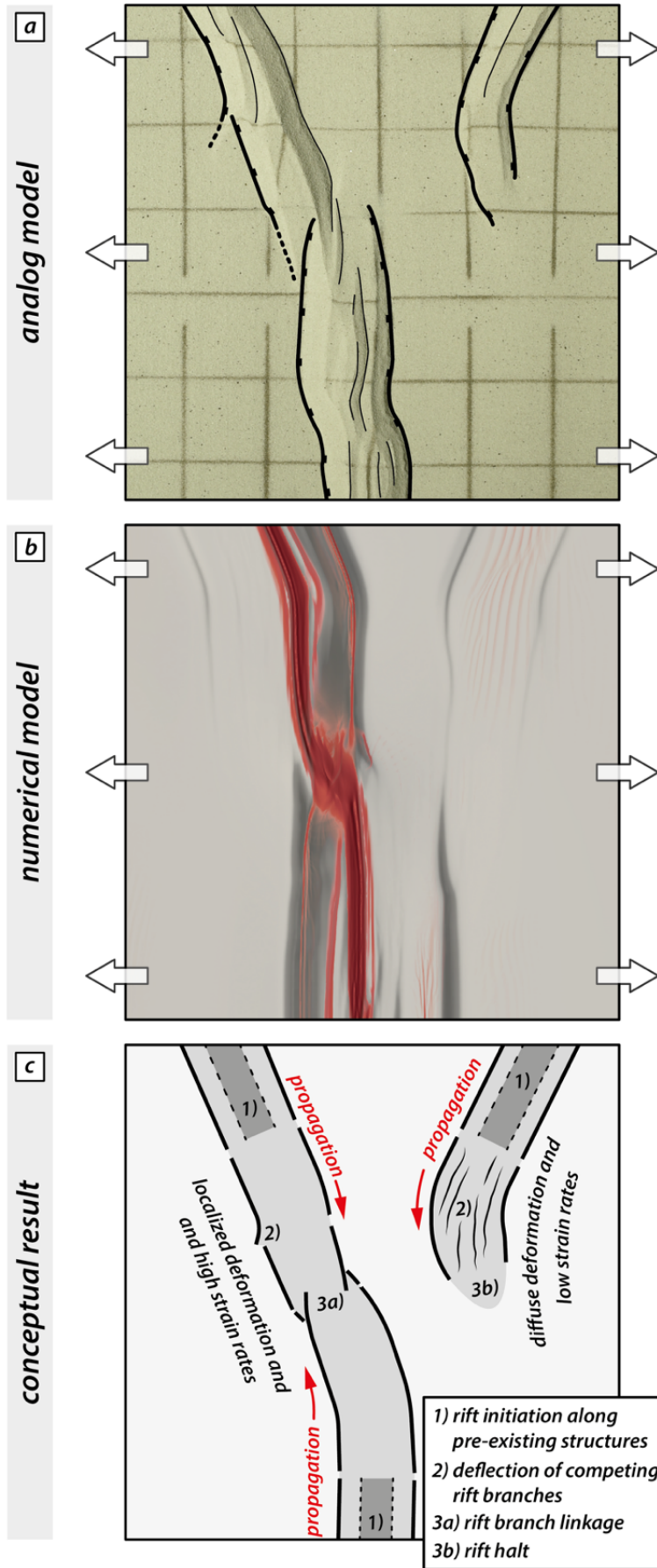
Figure 9: *Summary plot showing the geometric similarity of rift segment linkage, deflection of competing branches and abandonment in analog and numerical models. a) Observed key features at the final stage of the analog model. b) Final strain and strain rate pattern in the numerical reference model. c) Conceptual interpretation of rift deflection and linkage based on our analog and numerical results (for details see text).*

724

5. Conclusions

We present a series of analog and numerical rifting experiments. Our results suggest that, even in a relatively simple iso-viscous two-layer crustal setup, pre-existing weaknesses substantially disturb the regional stress pattern, which impacts rift propagation and the overall rift evolution. The complex stress re-orientation is distinct for different seed configurations (i.e., v-seed, i-seed, and y-seed) and closely interacts with the final rift geometry. The most important findings of our study can be summarized as follows:

- Our numerical experiments reproduce rift segment deflection seen in our analog models. This highlights the robustness of our results and their applicability to interpreting rift segment propagation, interaction, and linkage in natural settings of continental rifting.

- Pre-existing structures may control localization of rift segments that successively propagate into previously undeformed areas. Consequently, stress re-orientation initially occurs along pre-conditioned zones and propagates, coevally with rift segment propagation and strain accrual, into formerly undeformed areas.

- Interacting stresses between two competing rift segments may cause outward deflection of the propagating rift tips resulting in a successively broader rift geometry along-strike.

- Outward deflection of competing rift segments is less prominent if an opposingly propagating rift segment is present. With progressive extensional deformation, strain accrual along one of the competing rift segments prevails whilst faulting activity along the other segment ceases. Coevally, the general stress orientation changes from a symmetric to an asymmetric distribution indicating the onset of rift linkage.

- Our modelling results reproduce first-order structures of natural examples from the East African Rift System and, on smaller scale, graben structures in the Canyonlands

751   National Park. The combined investigation of surface stresses and strain localization

752   provides an explanation for distinct rift deflection among competing rift segments and

753   rift linkage structures where ongoing deformation and stresses mutually affect each

754   other.

755

756 While changes in rift orientation are often used to infer regional palaeo-movements, we

757 demonstrate that local stress field re-orientations can occur under constant plate motions.

758 Albeit on a smaller scale, implications from our observations corroborate findings from

759 previous studies (Brune; 2014; Duclaux et al., 2020; Gapais et al., 2000). Locally, stress and

760 strain can largely deviate from a regional, far-field pattern and instead represent local

761 deformation interference. In addition, the observed stress re-orientations change over time

762 indicating that stresses measured in natural examples may depict transient stages that change

763 with progressive deformation due to subsequent changes in material strengths (Morley et al.,

764 2004). This implication must be considered in processing local fault-slip data when interpreting

765 the evolution of rifts at any scale.

Data availability

Rheological measurements of the used analog materials are available in the form of open access data publications provided by the GFZ Data Service (brittle materials: Schmid et al., 2020a; Schmid et al., 2020b; viscous materials: Zwaan et al., 2018).

Acknowledgements

We thank Esther Heckenbach for helpful assistance with post processing and visualization. The work was supported by the North-German Supercomputing Alliance (HLRN). We thank the Swiss National Science Foundation for providing financial support. Finally, we thank the two reviewers, Guillaume Duclaux and Chris Morley for their detailed, constructive and motivating comments that significantly helped to improve this manuscript.

Funding

This project is supported by the Swiss National Science Foundation [grant number 200021_178731].

CRediT authorship contribution statement

Timothy C. Schmid: Conceptualization, Methodology, Investigation, Formal Analysis, Writing – original draft, Visualization, Data curation. Sascha Brune: Conceptualization, Methodology, HPC funding acquisition, Supervision, Project administration, Writing – review & editing. Anne Glerum: Methodology, Software, HPC funding acquisition, Writing – review & editing. Guido Schreurs: Writing – review & editing, Supervision, Project administration, Funding acquisitions, Resources.

References

Abebe, T., Mazzarini, F., Innocenti, F., and Manetti, P.: The Yerer-Tullu Wellel volcanotectonic lineament: A transtensional structure in central Ethiopia and the associated magmatic activity, Journal of African Earth Sciences, 26, 135-150, 1998.
https://doi.org/10.1016/S0899-5362(97)00141-3

Acocella, V., Faccenna, C., Funiciello, R., and Rossetti, F.: Sand-box modelling of basement-controlled transfer zones in extensional domains, Terra Nova-Oxford, 11, 149-156, 1999.

Adam, J., Urai, J., Wieneke, B., Oncken, O., Pfeiffer, K., Kukowski, N., Lohrmann, J., Hoth, S., Van Der Zee, W., and Schmatz, J.: Shear localisation and strain distribution during tectonic faulting—New insights from granular-flow experiments and high-resolution optical image correlation techniques, Journal of Structural Geology, 27, 283-301, 2005.
https://doi.org/10.1016/j.jsg.2004.08.008

Allken, V., Huismans, R. S., and Thieulot, C.: Three-dimensional numerical modeling of upper crustal extensional systems, Journal of Geophysical Research: Solid Earth, 116, 2011.
https://doi.org/10.1029/2011JB008319

Allken, V., Huismans, R. S., and Thieulot, C.: Factors controlling the mode of rift interaction in brittle-ductile coupled systems: A 3D numerical study, Geochemistry, Geophysics, Geosystems, 13, 2012.
https://doi.org/10.1029/2012GC004077

Allken, V., Huismans, R. S., Fossen, H., and Thieulot, C.: 3D numerical modelling of graben interaction and linkage: a case study of the Canyonlands grabens, Utah, Basin Research, 25, 436-449, 2013.
https://doi.org/10.1111/bre.12010

Anderson, E. M.: The dynamics of faulting, Transactions of the Edinburgh Geological Society, 8, 387-402, 1905.
https://doi.org/10.1144/transed.8.3.387

Bellahsen, N. and Daniel, J. M.: Fault reactivation control on normal fault growth: an experimental study, Journal of Structural Geology, 27, 769-780, 2005.
https://doi.org/10.1016/j.jsg.2004.12.003

Bonini, M., Corti, G., Innocenti, F., Manetti, P., Mazzarini, F., Abebe, T., and Pecskay, Z.: Evolution of the Main Ethiopian Rift in the frame of Afar and Kenya rifts propagation, Tectonics, 24, 2005.
https://doi.org/10.1029/2004TC001680

Bosworth, W.: Geometry of propagating continental rifts, Nature, 316, 625-627, 1985.
https://doi.org/10.1038/316625a0

Brune, S.: Evolution of stress and fault patterns in oblique rift systems: 3-D numerical lithospheric-scale experiments from rift to breakup, Geochemistry, Geophysics, Geosystems, 15, 3392-3415, 2014.
https://doi.org/10.1002/2014GC005446

Brune, S. and Autin, J.: The rift to break-up evolution of the Gulf of Aden: Insights from 3D numerical lithospheric-scale modelling, Tectonophysics, 607, 65-79, 10.1016/j.tecto.2013.06.029, 2013.
https://doi.org/10.1016/j.tecto.2013.06.029

Brune, S., Corti, G., and Ranalli, G.: Controls of inherited lithospheric heterogeneity on rift linkage: Numerical and analog models of interaction between the Kenyan and Ethiopian rifts across the Turkana depression, Tectonics, 36, 1767-1786, 2017.
https://doi.org/10.1002/2017TC004739

Brune, S., Popov, A. A., and Sobolev, S. V.: Modeling suggests that oblique extension facilitates rifting and continental break-up, Journal of Geophysical Research: Solid Earth, 117, 2012.
https://doi.org/10.1029/2011JB008860

Childs, C., Watterson, J., and Walsh, J.: Fault overlap zones within developing normal fault systems, Journal of the Geological Society, 152, 535-549, 1995.
https://doi.org/10.1144/gsjgs.152.3.0535

852   Collanega, L., Jackson, C. A.-L., Bell, R., Coleman, A. J., Lenhart, A., and Breda, A.: How do intra-basement fabrics
853   influence normal fault growth? Insights from the Taranaki Basin, offshore New Zealand, 2018.
854   https://doi.org/10.31223/osf.io/8rn9u
855
856   Corti, G.: Evolution and characteristics of continental rifting: Analog modeling-inspired view and comparison with
857   examples from the East African Rift System, Tectonophysics, 522-523, 1-33, 10.1016/j.tecto.2011.06.010, 2012.
858   https://doi.org/10.1016/j.tecto.2011.06.010
859
860   Corti, G., van Wijk, J., Cloetingh, S., and Morley, C. K.: Tectonic inheritance and continental rift architecture:
861   Numerical and analogue models of the East African Rift system, Tectonics, 26, 2007.
862   https://doi.org/10.1029/2006TC002086
863
864   Corti, G., Philippon, M., Sani, F., Keir, D., and Kidane, T.: Re-orientation of the extension direction and pure
865   extensional faulting at oblique rift margins: Comparison between the Main Ethiopian Rift and laboratory
866   experiments, Terra Nova, 25, 396-404, 2013.
867   https://doi.org/10.1111/ter.12049
868
869   Corti, G., Cioni, R., Franceschini, Z., Sani, F., Scaillet, S., Molin, P., Isola, I., Mazzarini, F., Brune, S., and Keir, D.:
870   Aborted propagation of the Ethiopian rift caused by linkage with the Kenyan rift, Nature communications, 10, 1-
871   11, 2019.
872   https://doi.org/10.1038/s41467-019-09335-2
873
874   Crameri, F., Shephard, G. E., and Heron, P. J.: The misuse of colour in science communication, Nature
875   communications, 11, 1-10, 2020.
876   https://doi.org/10.1038/s41467-020-19160-7
877
878   Daly, M., Chorowicz, J., and Fairhead, J.: Rift basin evolution in Africa: the influence of reactivated steep basement
879   shear zones, Geological Society, London, Special Publications, 44, 309-334, 1989.
880   https://doi.org/10.1144/GSL.SP.1989.044.01.17
881
882   Duclaux, G., Huismans, R. S., and May, D. A.: Rotation, narrowing, and preferential reactivation of brittle structures
883   during oblique rifting, Earth and Planetary Science Letters, 531, 115952, 2020.
884   https://doi.org/10.1016/j.epsl.2019.115952
885
886   Duffy, O. B., Bell, R. E., Jackson, C. A.-L., Gawthorpe, R. L., and Whipp, P. S.: Fault growth and interactions in a
887   multiphase rift fault network: Horda Platform, Norwegian North Sea, Journal of Structural Geology, 80, 99-119,
888   2015.
889   https://doi.org/10.1016/j.jsg.2015.08.015
890
891   Duretz, T., de Borst, R., and Le Pourhiet, L.: Finite thickness of shear bands in frictional viscoplasticity and
892   implications for lithosphere dynamics, Geochemistry, Geophysics, Geosystems, 20, 5598-5616, 2019.
893   https://doi.org/10.1029/2019GC008531
894
895   Ebinger, C., Yemane, T., Harding, D., Tesfaye, S., Kelley, S., and Rex, D.: Rift deflection, migration, and
896   propagation: Linkage of the Ethiopian and Eastern rifts, Africa, Geological Society of America Bulletin, 112, 163-
897   176, 2000.
898   https://doi.org/10.1130/0016-7606(2000)112<163:RDMAPL>2.0.CO;2
899
900   Gapais, D., Cobbold, P. R., Bourgeois, O., Rouby, D., and de Urreiztieta, M.: Tectonic significance of fault-slip data,
901   Journal of Structural Geology, 22, 881-888, 2000.
902   https://doi.org/10.1016/S0191-8141(00)00015-8
903
904   Gassmöller, R., Lokavarapu, H., Heien, E., Puckett, E. G., and Bangerth, W.: Flexible and scalable particle-in-cell
905   methods with adaptive mesh refinement for geodynamic computations, Geochemistry, Geophysics, Geosystems,
906   19, 3596-3604, 2018.
907   https://doi.org/10.1029/2018GC007508
908
909   Glerum, A., Brune, S., Stamps, D. S., and Strecker, M. R.: Victoria continental microplate dynamics controlled by
910   the lithospheric strength distribution of the East African Rift, Nature Communications, 11, 1-15, 2020.
911   https://doi.org/10.1038/s41467-020-16176-x
912
913   Glerum, A., Thieulot, C., Fraters, M., Blom, C., and Spakman, W.: Nonlinear viscoplasticity in ASPECT:
914   benchmarking and applications to subduction, Solid Earth, 9, 267-294, 2018.
915   https://doi.org/10.5194/se-9-267-2018

Gudmundsson, A., Simmenes, T. H., Larsen, B., and Philipp, S. L.: Effects of internal structure and local stresses on fracture propagation, deflection, and arrest in fault zones, Journal of Structural Geology, 32, 1643-1655, 2010. https://doi.org/10.1016/j.jsg.2009.08.013

Heidbach, O., Rajabi, M., Cui, X., Fuchs, K., Müller, B., Reinecker, J., Reiter, K., Tingay, M., Wenzel, F., and Xie, F.: The World Stress Map database release 2016: Crustal stress pattern across scales, Tectonophysics, 744, 484-498, 2018. https://doi.org/10.1016/j.tecto.2018.07.007

Heilman, E., Kolawole, F., Atekwana, E. A., and Mayle, M.: Controls of Basement Fabric on the Linkage of Rift Segments, Tectonics, 38, 1337-1366, 10.1029/2018tc005362, 2019. https://doi.org/10.1029/2018TC005362

Heister, T., Dannberg, J., Gassmöller, R., and Bangerth, W.: High accuracy mantle convection simulation through modern numerical methods–II: realistic models and problems, Geophysical Journal International, 210, 833-851, 2017. https://doi.org/10.1029/2018TC005362

Jacquey, A. B. and Cacace, M.: Multiphysics modeling of a brittle-ductile lithosphere: 2. Semi-brittle, semi-ductile deformation and damage rheology, Journal of Geophysical Research: Solid Earth, 125, e2019JB018475, 2020. https://doi.org/10.1029/2019JB018475

Kattenhorn, S. A., Aydin, A., and Pollard, D. D.: Joints at high angles to normal fault strike: an explanation using 3-D numerical models of fault-perturbed stress fields, Journal of structural Geology, 22, 1-23, 2000. https://doi.org/10.1016/S0191-8141(99)00130-3

Katzman, R., ten Brink, U. S., and Lin, J.: Three-dimensional modeling of pull-apart basins: Implications for the tectonics of the Dead Sea Basin, Journal of Geophysical Research: Solid Earth, 100, 6295-6312, 1995. https://doi.org/10.1029/94JB03101

Keranen, K. and Klemperer, S.: Discontinuous and diachronous evolution of the Main Ethiopian Rift: Implications for development of continental rifts, Earth and Planetary Science Letters, 265, 96-111, 2008. https://doi.org/10.1016/j.epsl.2007.09.038

Koehn, D., Aanyu, K., Haines, S., and Sachau, T.: Rift nucleation, rift propagation and the creation of basement micro-plates within active rifts, Tectonophysics, 458, 105-116, 2008. https://doi.org/10.1016/j.tecto.2007.10.003

Kolawole, F., Phillips, T. B., Atekwana, E. A., and Jackson, C. A.-L.: Structural inheritance controls strain distribution during early continental rifting, rukwa rift, Frontiers in Earth Science, 670, 2021. https://doi.org/10.3389/feart.2021.707869

Kolawole, F., Atekwana, E. A., Laó-Dávila, D. A., Abdelsalam, M. G., Chindandali, P. R., Salima, J., and Kalindekafe, L.: Active Deformation of Malawi Rift's North Basin Hinge Zone Modulated by Reactivation of Preexisting Precambrian Shear Zone Fabric, Tectonics, 37, 683-704, 10.1002/2017tc004628, 2018. https://doi.org/10.1002/2017TC004628

Kronbichler, M., Heister, T., and Bangerth, W.: High accuracy mantle convection simulation through modern numerical methods, Geophysical Journal International, 191, 12-29, 2012. https://doi.org/10.1111/j.1365-246X.2012.05609.x

Lavier, L. L., Buck, W. R., and Poliakov, A. N.: Factors controlling normal fault offset in an ideal brittle layer, Journal of Geophysical Research: Solid Earth, 105, 23431-23442, 2000. https://doi.org/10.1029/2000JB900108

Macdonald, K. C. and Fox, P.: Overlapping spreading centres: New accretion geometry on the East Pacific Rise, Nature, 302, 55-58, 1983. https://doi.org/10.1038/302055a0

Mills, N.: Dislocation array elements for the analysis of crack and yielded zone growth, Journal of Materials Science, 16, 1317-1331, 1981. https://doi.org/10.1007/BF01033848

979 Mondy, L. S., Rey, P. F., Duclaux, G., and Moresi, L.: The role of asthenospheric flow during rift propagation and
980 breakup, Geology, 46, 103-106, 2018.
981 https://doi.org/10.1130/G39674.1

983 Morley, C.: Stress re-orientation along zones of weak fabrics in rifts: An explanation for pure extension in 'oblique'
984 rift segments?, Earth and Planetary Science Letters, 297, 667-673, 2010.
985 https://doi.org/10.1016/j.epsl.2010.07.022

987 Morley, C.: The impact of multiple extension events, stress rotation and inherited fabrics on normal fault geometries
988 and evolution in the Cenozoic rift basins of Thailand, Geological Society, London, Special Publications, 439, 413-
989 445, 2017.
990 https://doi.org/10.1144/SP439.3

992 Morley, C., Nelson, R., Patton, T., and Munn, S.: Transfer zones in the East African rift system and their relevance
993 to hydrocarbon exploration in rifts, AAPG bulletin, 74, 1234-1253, 1990.
994 https://doi.org/10.1306/0C9B2475-1710-11D7-8645000102C1865D

996 Morley, C., Haranya, C., Phoosongsee, W., Pongwapee, S., Kornsawan, A., and Wonganan, N.: Activation of rift
997 oblique and rift parallel pre-existing fabrics during extension and their effect on deformation style: examples from
998 the rifts of Thailand, Journal of Structural Geology, 26, 1803-1829, 2004.
999 https://doi.org/10.1016/j.jsg.2004.02.014

1001 Morley, C. K.: Patterns of displacement along large normal faults: implications for basin evolution and fault
1002 propagation, based on examples from East Africa, AAPG bulletin, 83, 613-634, 1999.
1003 https://doi.org/10.1306/00AA9C0A-1730-11D7-8645000102C1865D

1005 Muhabaw, Y., Muluneh, A. A., Nugsse, K., Gebru, E. F., and Kidane, T.: Paleomagnetism of Gedemsa magmatic
1006 segment, Main Ethiopian Rift: Implication for clockwise rotation of the segment in the Early Pleistocene,
1007 Tectonophysics, 838, 229475, 2022.
1008 https://doi.org/10.1016/j.tecto.2022.229475

1010 Nelson, R., Patton, T., and Morley, C.: Rift-segment interaction and its relation to hydrocarbon exploration in
1011 continental rift systems, AAPG bulletin, 76, 1153-1169, 1992.
1012 https://doi.org/10.1306/BDFF898E-1718-11D7-8645000102C1865D

1014 Oliva, S. J., Ebinger, C. J., Rivalta, E., Williams, C. A., Wauthier, C., and Currie, C. A.: State of stress and stress
1015 rotations: Quantifying the role of surface topography and subsurface density contrasts in magmatic rift zones
1016 (Eastern Rift, Africa), Earth and Planetary Science Letters, 584, 117478, 2022.
1017 https://doi.org/10.1016/j.epsl.2022.117478

1019 Philippon, M., Willingshofer, E., Sokoutis, D., Corti, G., Sani, F., Bonini, M., and Cloetingh, S.: Slip re-orientation in
1020 oblique rifts, Geology, 43, 147-150, 2015.
1021 https://doi.org/10.1130/G36208.1

1023 Pollard, D. D. and Aydin, A.: Propagation and linkage of oceanic ridge segments, Journal of Geophysical Research:
1024 Solid Earth, 89, 10017-10028, 1984.
1025 https://doi.org/10.1029/JB089iB12p10017

1027 Rose, I., Buffett, B., and Heister, T.: Stability and accuracy of free surface time integration in viscous flows, Physics
1028 of the Earth and Planetary Interiors, 262, 90-100, 2017.
1029 https://doi.org/10.1016/j.pepi.2016.11.007

1031 Rosendahl, B. R.: Architecture of continental rifts with special reference to East Africa, Annual Review of Earth and
1032 Planetary Sciences, 15, 445, 1987.
1033 https://doi.org/10.1146/annurev.ea.15.050187.002305

1035 Saria, E., Calais, E., Stamps, D., Delvaux, D., and Hartnady, C.: Present-day kinematics of the East African Rift,
1036 Journal of Geophysical Research: Solid Earth, 119, 3584-3600, 2014.
1037 https://doi.org/10.1002/2013JB010901

1039 Schmid, T., Schreurs, G., Warsitzka, M., and Rosenau, M.: Effect of sieving height on density and friction of brittle
1040 analogue material: ring-shear test data of quarz sand used for analogue experiments in the Tectonic Modelling Lab
1041 of the University of Bern, 2020a.
1042 https://doi.org/10.5880/fidgeo.2020.006

1043 Schmid, T., Schreurs, G., Warsitzka, M., and Rosenau, M.: Effect of sieving height on density and friction of brittle
1044 analogue material: Ring-shear test data of corundum sand used for analogue experiments in the Tectonic Modelling
1045 Lab of the University of Bern (CH), 2020b.
1046 https://doi.org/10.5880/fidgeo.2020.005
1047
1048 Schultz-Ela, D. and Walsh, P.: Modeling of grabens extending above evaporites in Canyonlands National Park, Utah,
1049 Journal of Structural Geology, 24, 247-275, 2002.
1050 https://doi.org/10.1016/S0191-8141(01)00066-9
1051
1052 Tingay, M., Muller, B., Reinecker, J., and Heidbach, O.: State and origin of the present-day stress field in
1053 sedimentary basins: New results from the World Stress Map Project, Golden Rocks 2006, The 41st US Symposium
1054 on Rock Mechanics (USRMS).
1055
1056 Tingay, M. R., Morley, C. K., Hillis, R. R., and Meyer, J.: Present-day stress orientation in Thailand's basins, Journal
1057 of Structural Geology, 32, 235-248, 2010.
1058 https://doi.org/10.1016/j.jsg.2009.11.008
1059
1060 Tron, V. and Brun, J.-P.: Experiments on oblique rifting in brittle-ductile systems, Tectonophysics, 188, 71-84,
1061 1991.
1062 https://doi.org/10.1016/0040-1951(91)90315-J
1063
1064 Trudgill, B. D.: Structural controls on drainage development in the Canyonlands grabens of southeast Utah, AAPG
1065 bulletin, 86, 1095-1112, 2002.
1066 https://doi.org/10.1306/61EEDC2E-173E-11D7-8645000102C1865D
1067
1068 Willemse, E. J.: Segmented normal faults: Correspondence between three-dimensional mechanical models and
1069 field data, Journal of Geophysical Research: Solid Earth, 102, 675-692, 1997.
1070 https://doi.org/10.1029/96JB01651
1071
1072 Willemse, E. J., Pollard, D. D., and Aydin, A.: Three-dimensional analyses of slip distributions on normal fault arrays
1073 with consequences for fault scaling, Journal of Structural Geology, 18, 295-309, 1996.
1074 https://doi.org/10.1016/S0191-8141(96)80051-4
1075
1076 Withjack, M. O. and Jamison, W. R.: Deformation produced by oblique rifting, Tectonophysics, 126, 99-124, 1986.
1077 https://doi.org/10.1016/0040-1951(86)90222-2
1078
1079 Zoback, M. L.: First-and second-order patterns of stress in the lithosphere: The World Stress Map Project, Journal
1080 of Geophysical Research: Solid Earth, 97, 11703-11728, 1992.
1081 https://doi.org/10.1029/92JB00132
1082
1083 Zwaan, F. and Schreurs, G.: How oblique extension and structural inheritance influence rift segment interaction:
1084 Insights from 4D analog models, Interpretation, 5, SD119-SD138, 2017.
1085 https://doi.org/10.1190/INT-2016-0063.1
1086
1087 Zwaan, F., Schreurs, G., Naliboff, J., and Buiter, S. J. H.: Insights into the effects of oblique extension on continental
1088 rift interaction from 3D analogue and numerical models, Tectonophysics, 693, 239-260,
1089 10.1016/j.tecto.2016.02.036, 2016.
1090 https://doi.org/10.1016/j.tecto.2016.02.036
1091
1092 Zwaan, F., Schreurs, G., Ritter, M., Santimano, T., and Rosenau, M.: Rheology of PDMS-corundum sand mixtures
1093 from the Tectonic Modelling Lab of the University of Bern (CH), 2018.
1094 http://doi.org/10.5880/fidgeo.2018.023
1095
1096